



# Modeling of a solution polymerization reactor operating in semi-batch mode for polymethyl methacrylate production

Fermín Sáez-Pardo, Juan José Giner-Sanz\*, Montserrat García-Gabaldón, Valentín Pérez-Herranz

IEC group, Depto. Ingeniería Química y Nuclear, Universitat Politècnica de València, Camí de Vera s/n, Valencia 46022, Spain

## ARTICLE INFO

### Keywords:

Polymerization reactor modelling  
Polymethyl methacrylate  
Semi-batch operation  
Simulation  
Solution polymerization

## ABSTRACT

The severe consequences of thermal runaways, make process optimization of paramount importance for free radical polymerization reactors, in order to maximize in an integrated way their safety and productivity. Generally, this optimization is performed by simulation, for the sake of safety and cost. Today, the literature contains several models of free radical polymerization reactors in general; and methyl methacrylate (MMA) polymerization reactors, in particular. Although, MMA polymerization is commonly performed in semi-batch reactors at industrial level, most of the available models focus on batch reactors; while, the semi-batch reactor models are much scarcer. In this work, a model of a MMA solution polymerization batch reactor was modified in order to generalize it to semi-batch operation. The developed semi-batch model was used here for studying the effect of different operation conditions (feeding flow rate, initiator load, monomer initial load, and reactor temperature) on the quality characteristics of the produced polymer and on the safety and productivity of the polymerization reactor. The developed model can be used to optimize the operation conditions of a semi-batch reactor so that the final product quality meets the application requirements, while maintaining the reactor within its safe-operation envelope, and maximizing its productivity.

## 1. Introduction

Polymethyl methacrylate (PMMA) is a polymer widely used nowadays to produce acrylic plastic (Li et al., 2022a). PMMA displays excellent optical and mechanical properties: it has high strength, dimensional stability and weathering resistance, as well as an outstanding optical clarity (Zhan et al., 2022). Owing to its excellent properties, PMMA is used today in a wide range of applications in which its toughness, rigidity and transparency justify its price (Brydson, 1999; Baxter and Yeh, 2012). The fields in which PMMA is being used nowadays include building materials (Sun et al., 2021), microfluidics (Guo et al., 2020; Duan et al., 2020; Zhang et al., 2020; Ahn et al., 2020), energy harvest (Ding et al., 2020) and storage (Zhao et al., 2021; Zhou et al., 2020; Li et al. (2020a); Mao et al., 2022; Liu et al., 2022; Li et al., 2022b; Bao et al., 2021), photonic crystals (Fan et al., 2022; Chen et al., 2021; Li et al., 2021; Xie et al., 2021), solar cells and reactors (Wang et al., 2021; Zhao et al., 2020), chemical and biological reactors (Li et al., 2020a; Ren et al., 2020), biomedicine (Fu et al., 2020; Gao et al., 2020), optical and electronic devices (Kwon and Myoung, 2020; Ma

et al., 2021; Xu et al., 2021), and 3D printing (Li et al., 2020b), amongst many others.

PMMA is produced by methyl methacrylate (MMA) polymerization, predominantly by the free radical mechanism (Arora et al., 2010; Goseki and Ishizone, 2014). Thermally initiated polymerization of MMA can be performed homogeneously, by bulk or solution polymerization; or heterogeneously, by suspension or emulsion polymerization (Serrano-Aroca and Deb, 2020). The polymerization method depends on the application of the polymer (Stickler and Rhein, 1992). Bulk polymerization is the predominant method for producing high quality acrylic glass, such as Plexiglas®. Solution polymerization is used in industry for producing adhesives, paint resins, and additives. Suspension polymerization is used for producing PMMA beads, which can then be molded. And finally, emulsion polymerization is used to produce paint resins, paper coating agents and paper processing agents, textile binders, and additives.

Free radical polymerizations are one of the most frequent causes of thermal runaway events in the chemical industry (Nolan and Barton, 1987), mainly because of the high exothermicity of these polymerization

\* Corresponding author.

E-mail address: [juagisan@etsii.upv.es](mailto:juagisan@etsii.upv.es) (J.J. Giner-Sanz).

<https://doi.org/10.1016/j.cherd.2024.08.024>

Received 7 March 2024; Received in revised form 4 July 2024; Accepted 20 August 2024

Available online 26 August 2024

0263-8762/© 2024 The Authors. Published by Elsevier Ltd on behalf of Institution of Chemical Engineers. This is an open access article under the CC BY-NC-ND license (<http://creativecommons.org/licenses/by-nc-nd/4.0/>).

reactions (up to 110 kJ·mol<sup>-1</sup> (Nolan and Barton, 1987)), and the Trommsdorff-Norrish autoacceleration effect (Copelli et al., 2019; Crowley and Choi, 1996; Gyax, 1988). In addition, undesired secondary reactions, such as chain transfer to monomer, backbiting and propagation of tertiary radicals may occur, increasing the tendency to thermal runaway (Bosch et al., 2004; Ampelli et al., 2006). If high temperatures are reached during the runaway, cross-linking phenomena are triggered (Copelli et al., 2011) and boiling may occur inside the reactor (causing an overpressure), which can cause the irreparable loss of the entire polymerization reactor body, and in some extreme cases, explosions that can damage partially, or totally, the production plant. Such thermal runaway events have been responsible for a large number of accidents in chemical plants (Cassona et al., 2014; Casson et al., 2014; Casson and Maschio, 2011; Moreno et al., 2016).

The severe consequences of thermal runaways, make process optimization of paramount importance for free radical polymerization reactors, in order to maximize in an integrated way their safety and productivity. Although this optimization process can be achieved experimentally, it usually carries large safety issues and economic costs. In this context, simulation emerges as a great tool for reactor operation optimization without the drawbacks of the experimental optimization strategy (safety and cost). However, in order to be able to achieve a reliable optimization of the reactor operation, it is essential to develop accurate models that capture all the complex physical phenomena that take place in free radical polymerizations, such as gel, glass and cage effects. In order to be useful for reactor operation optimization, a model should be able to simulate the effect of the different operation parameters of the reactor: mainly the reactor load, the reactor temperature, and the dosing strategy. As of today, several of such models can be found in literature (Copelli et al., 2018), for instance for styrene emulsion polymerization (Zubov et al., 2012; Pokorný et al., 2016) and for vinyl acetate polymerization (Arora et al., 2005; Gil et al., 2016). In the case of MMA polymerization, models have been proposed for bulk polymerization (Achilias and Kiparissides, 1992; Nising, 2006; Wu and Shan, 2006; Baillagou and Soong, 1985), for solution polymerization (Baillagou and Soong, 1985; Louie et al., 1985; Crowley and Choi, 1997; Ahn et al., 1998; Law et al., 2016), for suspension polymerization (Kalfas and Ray, 1993; Kalfas et al., 1993; Shahrokhi and Fanaei, 2002), and for emulsion polymerization (Rawlings and Ray, 1988; Gao and Penlidis, 2002). MMA polymerization is commonly performed in semi-batch reactors at industrial level (Ghosh et al., 1998), since this operation mode allows a better temperature control, and therefore a safer operation (Copelli et al., 2018). However, while a great number of the available models focus on reactors operating in batch mode; the semi-batch reactor models are much scarcer. Some works have proposed models for semi-batch reactors for MMA bulk (Wu and Shan, 2006) and emulsion polymerization (Ibrahim et al., 2011), but MMA semi-batch solution polymerization has not yet been addressed.

In this panorama, the goal of this work is the development of a model of a reactor operating in semi-batch mode for solution MMA polymerization. The developed model allows to predict the time evolution of both, important quality characteristics of the produced polymer such as the polymer's average molecular weight (Prentice, 1983) and its molar-mass dispersity (Sheu, 2001); and safety related parameters such as the generated thermal power. The model was used here for studying the effect of different operation conditions (feeding flow rate, initiator load, monomer initial load, and reactor temperature) on the quality characteristics of the produced PMMA and on the safety of the polymerization reactor. The obtained results can be used in order to optimize the dosing strategy of the semi-batch reactor so that the product quality is suitable, while maintaining the reactor within its safe-operation envelope.

## 2. Mathematical model

### 2.1. System description

In this work, a reactor operating in semi-batch mode for MMA solution polymerization was considered (Fig. 1). The reactor operates in a 5-state cycle. Initially, the reactor is in its idle state. During the startup step, the initiator load and an initial load of monomer are introduced in the polymerization reactor. Note that all the initiator is added to the reactor during the startup step, whereas only a fraction of the total monomer load is added. Both, the initiator and the monomer are added in solution with the solvent. As soon as the startup step is done, the feeding step starts: during this step, the monomer is fed to the reactor at a constant flow rate (i.e. as a solution of the monomer in the solvent), until the whole monomer load is introduced in the reactor (i.e. end of feeding). Once the end of feeding is reached, no more reactants are introduced in the reactor, where the reaction continues to take place for a given reaction time, after which the reactor is unloaded (i.e. unloading step). Once the reactor comes back to the idle step, it is ready to start the cycle again.

The considered polymerization reactor has a very good temperature control system that ensure an isothermal operation of the reactor: the temperature is considered constant (and equal to the selected reaction temperature) throughout the whole cycle.

The control volume considered in this work is the reactant mixture. For modelling purposes, here, this control volume is considered to be divided in 2 “virtual compartments”: a reactant compartment and a non-reactant compartment (that add up to the total control volume). The first one contains all the monomer, the initiator, the live polymer chains (i.e. growing chains) and the dead polymer chains; while, the second one contains the solvent.

### 2.2. Reaction mechanism and rate equations

The reaction mechanism (Table 1) considered in this work for MMA polymerization consists of the well-known 5-steps of free radical polymerization (Tefera et al., 1997): activation, initiation, propagation, termination, and chain transfer. First, during the activation step (R1), an initiator molecule (I) breaks spontaneously into two radicals (R<sup>\*</sup>). Second, during the initiation step (R2), the free radical reacts with a monomer molecule (M) to generate a live polymer chain of length 1 (M<sub>1</sub><sup>\*</sup>). Third, during the propagation step (R3), a live polymer chain of length *i* (M<sub>*i*</sub><sup>\*</sup>) reacts with a monomer unit to generate a live polymer chain of length *i* + 1. Forth, during the termination step (R4 and R5), two live polymer chains react by combination (R4), forming a single dead polymer chain (N<sub>*i+j*</sub>); or by disproportionation (R5), forming two dead polymer chains. And finally, during the chain transfer step (R6 to R9), a live polymer chain reacts with a monomer molecule (R6), with a solvent molecule (R7), with an initiator molecule (R8), or with a dead polymer chain (R9) to generate a single dead polymer chain and the corresponding radical. Although all the reactions mentioned above are known to occur in the case of MMA polymerization (Wu and Shan, 2006), only reactions R1 to R5 were taken into account in this work, since the rates of reactions R6 to R9 are negligible in the case of MMA polymerization (Chiu et al., 1983).

On the one side, the kinetic constants of the activation step (R1), *k<sub>d</sub>*; and the initiation step (R2), *k<sub>i</sub>*, only depend on the temperature, and were modelled with an Arrhenius model (Tefera et al., 1997):

$$k_d = \Lambda_d \cdot \exp\left(\frac{-E_d}{R \cdot T}\right) \quad (1)$$

$$k_i = \Lambda_i \cdot \exp\left(\frac{-E_i}{R \cdot T}\right) \quad (2)$$

Where  $\Lambda$  denotes the pre-exponential factor, and  $E$ , the activation en-

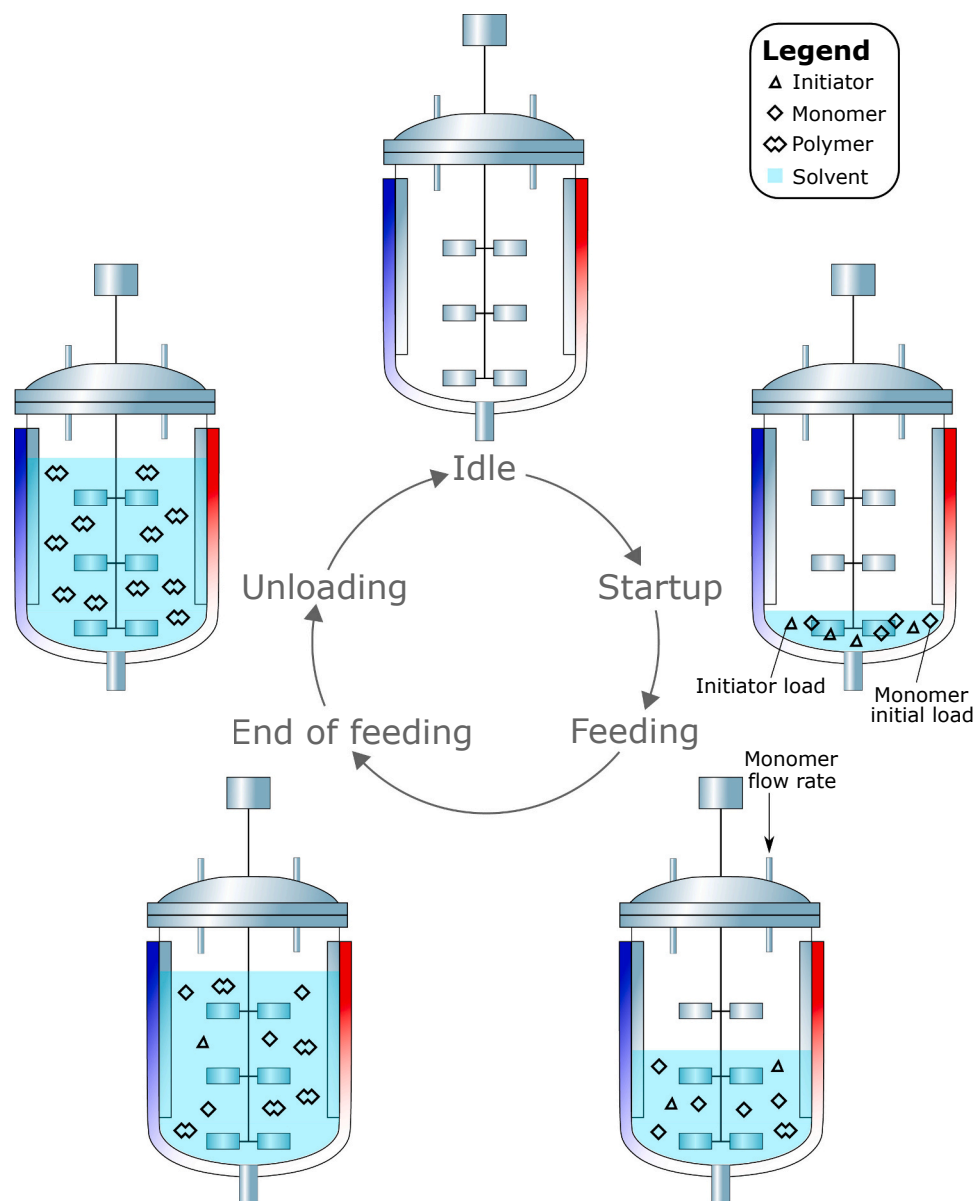


**Fig. 1.** Reactor operating in semi-batch mode for MMA solution polymerization. During the startup step, the initiator load and an initial load of monomer are introduced in the polymerization reactor. After that, monomer is fed to the reactor at a constant flow rate (i.e. feeding step), until the whole monomer load is introduced in the reactor (i.e. end of feeding). After this event, no more reactants are introduced in the reactor and the reaction continues in the reactor for a given polymerization time, after which the reactor is unloaded. Once the reactor comes back to the idle step, it is ready to start the cycle again.

**Table 1**

Kinetic scheme of MMA polymerization. The different symbols denote: I, initiator; R\*, radical; M, monomer; M<sub>i</sub><sup>\*</sup>, live polymer chain of length i; N<sub>i</sub>, dead polymer chain of length i; S, solvent; and S\*, solvent radical.

Id	Reaction name	Reaction
R1	Activation	$I \xrightarrow{k_{d1}} 2R^*$
R2	Initiation	$R^* + M \xrightarrow{k_{i1}} M_1^*$
R3	Propagation	$M_i^* + M \xrightarrow{k_{p1}} M_{i+1}^*$
R4	Termination by combination	$M_i^* + M_j^* \xrightarrow{k_{tc}} N_{i+j}$
R5	Termination by disproportionation	$M_i^* + M_j^* \xrightarrow{k_{td}} N_i + N_j$
R6	Chain transfer to monomer	$M_i^* + M \xrightarrow{k_{tm}} N_i + M_1^*$
R7	Chain transfer to solvent	$M_i^* + S \xrightarrow{k_{ts}} N_i + S^*$
R8	Chain transfer to initiator	$M_i^* + I \xrightarrow{k_{ti}} N_i + I^*$
R9	Chain transfer to polymer	$M_i^* + N_j \xrightarrow{k_{tp}} N_i + M_j^*$

ergy, of each one of the reactions.

On the other hand, the kinetic constants of the propagation step (R3),  $k_p$ ; and the termination step (R4 and R5),  $k_t$ , do not only depend on the temperature and require a more complex model, due to the gel effect that causes localized increases in viscosity of the polymerizing mixture that slow the termination reactions (i.e. diffusion-controlled termination) (Achilias and Kiparissides, 1988).

In order to represent the gel effect,  $k_p$  was modelled as a combination of two terms, the intrinsic kinetic constant (i.e. before the onset of the gel effect) and a diffusion related term (Chiu et al., 1983):

$$\frac{1}{k_p} = \frac{1}{k_p^0} + \frac{[M^*]}{k_{\theta p} \cdot \exp\left(\frac{2.3 \cdot \phi_m}{\alpha + \beta \cdot \phi_m}\right)} \quad (3)$$

The first term of the right-hand side of Eq. (3) corresponds with the propagation kinetic constant before the onset of the gel effect.  $k_p^0$  denotes the propagation kinetic constant at 0 monomer conversion (i.e. intrinsic

kinetic constant), that was modelled with an Arrhenius model (Law et al., 2016):

$$k_p^0 = A_p \cdot \exp\left(\frac{-E_p}{R \cdot T}\right) \quad (4)$$

The second term of the right-hand side of Eq. (3) captures the effect of diffusion limitations on the propagation kinetic constant (after the onset of the gel effect).  $[M^*]$  represents the sum of the concentrations of all the growing polymer chains (i.e. live polymers). Diffusion depends on temperature, chain length (i.e. molecular weight) and the number of polymer chains (i.e. conversion).  $k_{\theta p}$  captures the effect of the two first factors on the diffusion (Nising, 2006), and was modelled using an Arrhenius model (Law et al., 2016):

$$k_{\theta p} = A_{\theta p} \cdot \exp\left(\frac{-E_{\theta p}}{R \cdot T}\right) \quad (5)$$

The term  $\frac{[M^*]}{\exp\left(\frac{2.3 \cdot \phi_m}{\alpha + \beta \cdot \phi_m}\right)}$  corresponds to the conversion-related diffusion term, derived from the free volume (Howard, 1970) Fujita-Doolittle theory (Fujita et al., 1960).  $\phi_m$  denotes the monomer fraction in the reactant compartment (see Section 2.1) (Chiu et al., 1983):

$$\phi_m = \frac{1 - x}{1 + \epsilon \cdot x} \quad (6)$$

Where  $x$  represents the monomer conversion, and  $\epsilon$  is the volume expansion factor due to the fact that the polymer density ( $\rho_p$ ) is different to the monomer one ( $\rho_m$ ):

$$\epsilon = \frac{\rho_m - \rho_p}{\rho_p} \quad (7)$$

Finally,  $\alpha$  and  $\beta$  are temperature-dependent parameters (Chiu et al., 1983). However, numerous empirical works have shown that  $\beta$  is insensitive to temperature for many systems (Fujita et al., 1960), and MMA polymerization is one of such systems (Chiu et al., 1983). Consequently,  $\beta$  was considered constant in this work:  $\beta = 0.03$  (Baillagou and Soong, 1985). The temperature dependence of  $\alpha$  was modelled as (Law et al., 2016):

$$\alpha = \alpha_{gp} - \alpha_T \cdot (T - T_{gp})^2 \quad (8)$$

Where  $T_{gp}$  is the glass transition temperature of PMMA,  $\alpha_{gp}$  is the value at  $T_{gp}$  of the  $\alpha$  parameter of the Fujita-Doolittle equation, and  $\alpha_T$  is the temperature dependency coefficient of the  $\alpha$  parameter of the Fujita-Doolittle equation.

A similar gel effect model was used for the kinetic constant of the termination step (Chiu et al., 1983):

$$\frac{1}{k_t} = \frac{1}{k_t^0} + \frac{[M^*]}{k_{\theta t} \cdot \exp\left(\frac{2.3 \cdot \phi_m}{\alpha + \beta \cdot \phi_m}\right)} \quad (9)$$

Where both,  $k_t^0$  and  $k_{\theta t}$ , were modelled using an Arrhenius model (Law et al., 2016):

$$k_t^0 = A_t \cdot \exp\left(\frac{-E_t}{R \cdot T}\right) \quad (10)$$

$$k_{\theta t} = [I]_0 \cdot A_{\theta t} \cdot \exp\left(\frac{-E_{\theta t}}{R \cdot T}\right) \quad (11)$$

### 2.3. Mass balances

The total volume in the reactor can be divided in the volumes of the reactant and non-reactant compartments (see Section 2.1):

$$V_{tot} = V_r + V_{nr} \quad (12)$$

On the one side, the volume of the reactant compartment ( $V_r$ ), decreases as the reaction proceeds (Chiu et al., 1983):

$$V_r = V_{r0} \cdot (1 + \epsilon \cdot x) \quad (13)$$

Where  $V_{r0}$  denotes the initial volume of the reactant compartment. Deriving the above expression with respect to time:

$$\frac{dV_r}{dt} = Q_{er} \cdot (1 + \epsilon \cdot x) + \epsilon \cdot V_{r0} \cdot \frac{dx}{dt} \quad (14)$$

Where  $Q_{er}$  is the input reacting volumetric flow rate (i.e. the input volumetric flow rate excluding the solvent).

On the other side, the solvent molar balance yields:

$$\frac{dn_s}{dt} = Q_e \cdot [S]_e \quad (15)$$

Where  $n_s$  denotes the solvent moles in the reactor,  $Q_e$  is the input total volumetric flow rate, and  $[S]_e$  represents the solvent concentration in the input flow. The volume of the non-reactant compartment ( $V_{nr}$ ), can be obtained from  $n_s$ , the solvent molecular weight ( $PM_s$ ) and the solvent density ( $\rho_s$ ):

$$V_{nr} = \frac{n_s \cdot PM_s}{\rho_s} \quad (16)$$

Starting from the monomer's molar balance, the following expression was obtained:

$$\frac{dx}{dt} = -\frac{Q_e \cdot [M]_e}{[M]_0 \cdot V_{r0}} + k_p \cdot (1 - x) \cdot \left[ \sum_{i=1}^{\infty} [M_i^*] \right] + (1 - x) \cdot \frac{Q_{er}}{V_{r0}} \quad (17)$$

Where  $[M]_0$  denotes the monomer's initial concentration in the reactant compartment (calculated from the monomer's initial load), and  $[M]_e$  refers to the monomer's concentration in the input stream.

The initiator molar balance establishes that:

$$\frac{d[I]}{dt} = \frac{Q_e \cdot [I]_e}{V_r} - k_d \cdot [I] - \frac{[I]}{V_r} \cdot \frac{dV_r}{dt} \quad (18)$$

Where  $[I]_e$  ( $= 0 \text{ mol} \cdot \text{m}^{-3}$ , since initiator is not fed into the reactor during the feeding stage) denotes the initiator concentration in the input stream.

Finally, the live polymer molar balance yields:

$$\frac{dn_{M_i^*}}{dt} = \begin{cases} V_r \cdot (2 \cdot f \cdot k_d \cdot [I] - k_p \cdot [M_1^*] \cdot [M] - k_t \cdot [M_1^*] \cdot [M^*]) & \text{for } i = 1 \\ V_r \cdot (k_p \cdot [M] \cdot ([M_{i-1}^*] - [M_i^*]) - k_t \cdot [M_i^*] \cdot [M^*]) & \text{for } i > 1 \end{cases} \quad (19)$$

Where  $f$  denotes the initiator's factor of efficiency.

### 2.4. Polymer size distribution and its moments

In this work, the statistic moments method was used: instead of considering the whole polymer size distribution, the statistic moments were used to represent the distribution. The  $k^{\text{th}}$  statistic moment of the live polymer size distribution ( $\lambda_k$ ) and of the dead polymer size distribution ( $\mu_k$ ) are defined as:

$$\lambda_k = \sum_{i=1}^{\infty} i^k [M_i^*] \quad (20)$$

$$\mu_k = \sum_{i=1}^{\infty} i^k [N_i] \quad (21)$$

Combining the molar balances of the different species (see Section 2.3), the differential equations governing the time evolution of the 0<sup>th</sup>, the 1<sup>st</sup> and the 2<sup>nd</sup> statistic moment of the live polymer size distribution were obtained:

$$\frac{d\lambda_0}{dt} = 2 \cdot f \cdot k_d \cdot [I] - k_t \cdot \lambda_0^2 - \frac{\lambda_0}{V_r} \frac{dV_r}{dt} \quad (22)$$

$$\frac{d\lambda_1}{dt} = 2 \cdot f \cdot k_d \cdot [I] + k_p \cdot \lambda_0 \cdot [M] - k_t \cdot \lambda_0 \cdot \lambda_1 - \frac{\lambda_1}{V_r} \frac{dV_r}{dt} \quad (23)$$

$$\frac{d\lambda_2}{dt} = 2 \cdot f \cdot k_d \cdot [I] + k_p \cdot [M] \cdot (2 \cdot \lambda_1 + \lambda_0) - k_t \cdot \lambda_0 \cdot \lambda_2 - \frac{\lambda_2}{V_r} \frac{dV_r}{dt} \quad (24)$$

In this work, the initiator's factor of efficiency was considered constant, and therefore the proposed model only is valid for monomer conversions under 95 %: for higher conversions, the model predicts an endless increase of  $\lambda_0$ , which does not represent the real behavior of the system. This contradiction emerges from the assumption that the initiator's factor of efficiency is constant: for very low monomer concentrations (i.e. conversions above 95 %), the initiator's factor of efficiency is a function of the monomer conversion that tends to 0 as the monomer conversion tends to 1 (Wu and Shan, 2006). However, for monomer conversions below 95 % (i.e. the ones considered in this work), the constant factor of efficiency hypothesis is valid.

As with the live polymer case, the differential equations governing the time evolution of the 0<sup>th</sup>, the 1<sup>st</sup> and the 2<sup>nd</sup> statistic moment of the dead polymer size distribution were obtained:

$$\frac{d\mu_0}{dt} = k_t \cdot \lambda_0^2 - \frac{\mu_0}{V_r} \frac{dV_r}{dt} \quad (25)$$

$$\frac{d\mu_1}{dt} = k_t \cdot \lambda_1 \cdot \lambda_0 - \frac{\mu_1}{V_r} \frac{dV_r}{dt} \quad (26)$$

$$\frac{d\mu_2}{dt} = k_t \cdot \lambda_2 \cdot \lambda_0 - \frac{\mu_2}{V_r} \frac{dV_r}{dt} \quad (27)$$

The number-average ( $M_n$ ) and weight-average ( $M_w$ ) molecular weights of the polymer size distribution were obtained from the statistic moments and the monomer's molecular weight ( $PM_M$ ):

$$M_n = \frac{\lambda_1 + \mu_1}{\lambda_0 + \mu_0} \cdot PM_M \quad (28)$$

$$M_w = \frac{\lambda_2 + \mu_2}{\lambda_1 + \mu_1} \cdot PM_M \quad (29)$$

The molar-mass dispersity (PDI) was calculated using its IUPAC definition (Stepho, 2009):

$$PDI = \frac{M_w}{M_n} \quad (30)$$

## 2.5. Energy balance

The thermal power ( $\Psi$ ) generated in the reactor was modelled as:

$$\Psi = -\Delta H_r (k_p \cdot [M] + k_t \cdot [M^*]) \cdot [M^*] \cdot V_r \quad (31)$$

Where  $\Delta H_r$  denotes the reaction heat. In the above energy generation model only propagation and termination reactions were considered (i.e. the heat generation of reactions R1 and R2 was neglected).

Applying an energy balance to the reactor:

$$\frac{d(C_p \cdot V_{tot} \cdot \rho \cdot T)}{dt} = C_{p_e} \cdot Q_e \cdot \rho_e + \Psi - UA \cdot (T - T_j) \quad (32)$$

Where  $C_p$  and  $C_{p_e}$  denote the specific heat of the reactor's content and the inlet stream, respectively. In this work, the specific heats of the reactor content and the inlet stream (i.e. mixtures of different compounds) were calculated as the arithmetic weight fraction average of the pure component values (Poling et al., 2001). Although this hypothesis neglects any contribution due to the temperature variation of the enthalpy of mixing, its predictions for heat capacities of liquid mixtures are moderately accurate (Teja, 1983).  $\rho$  and  $\rho_e$  denote the density of the

reactor's content and the inlet stream, respectively.  $T$  is the temperature of the reactor, and  $T_j$  is the temperature of the refrigerant in the refrigeration jacket.  $U$  stands for the overall heat transfer coefficient and  $A$  is the heat exchange surface.

And finally, applying an energy balance to the refrigeration jacket:

$$\frac{dT_j}{dt} = \frac{Q_{ref}}{V_j} \cdot (T_{ref} - T_j) + UA \cdot \frac{T - T_j}{C_{p_{ref}} \cdot V_j \cdot \rho_{ref}} \quad (33)$$

Where  $Q_{ref}$  denotes the refrigerant volumetric flow rate,  $V_j$  is the volume of the refrigeration jacket,  $T_{ref}$  is the temperature of the refrigerant that enters the jacket, and  $C_{p_{ref}}$  and  $\rho_{ref}$  are the specific heat and the density of the refrigerant.

## 2.6. Model implementation

In this work, the model described in the previous sections was implemented in LabVIEW® 2021, using the Control Design and Simulation Module that provides tools to simulate dynamic systems in LabVIEW®. All the simulations performed in this work were carried out using a Runge-Kutta 4 fixed-step-size ODE solver, with a 0.1 second step size. Table 2 contains the values of the model parameters used in this work.

**Table 2**  
Model parameter values used in this work.

Parameter	Value	Units	Reference
Activation step activation energy ( $E_d$ )	128.77	$\text{kJ} \cdot \text{mol}^{-1}$	(Baillagou and Soong, 1985)
Activation step pre-exponential factor ( $\Lambda_d$ )	$1.0533 \cdot 10^{15}$	$\text{s}^{-1}$	(Baillagou and Soong, 1985)
Constant coefficient of the Fujita-Doolittle equation ( $\beta$ )	0.03	-	(Chiu et al., 1983)
Expansion factor ( $\epsilon$ )	-0.257	-	(Chiu et al., 1983)
Glass temperature ( $T_{gp}$ )	387.2	K	(Baillagou and Soong, 1985)
Initiation step activation energy ( $E_i$ )	18.283	$\text{kJ} \cdot \text{mol}^{-1}$	(Baillagou and Soong, 1985)
Initiation step pre-exponential factor ( $\Lambda_i$ )	491.67	$\text{m}^3 \cdot \text{mol}^{-1} \cdot \text{s}^{-1}$	(Baillagou and Soong, 1985)
Initiator efficiency factor ( $f$ )	0.58	-	(Tobolsky and Baysal, 1953)
Parameter $\alpha$ of the Fujita-Doolittle equation at glass temperature ( $\alpha_{gp}$ )	0.168	-	(Chiu et al., 1983)
Propagation step activation energy ( $E_p$ )	18.283	$\text{kJ} \cdot \text{mol}^{-1}$	(Baillagou and Soong, 1985)
Propagation step gel and glass effect activation energy ( $E_{gp}$ )	117.00	$\text{kJ} \cdot \text{mol}^{-1}$	(Baillagou and Soong, 1985)
Propagation step gel and glass effect pre-exponential factor ( $\Lambda_{gp}$ )	$3.0233 \cdot 10^{13}$	$\text{s}^{-1}$	(Baillagou and Soong, 1985)
Propagation step pre-exponential factor ( $\Lambda_p$ )	491.67	$\text{m}^3 \cdot \text{mol}^{-1} \cdot \text{s}^{-1}$	(Baillagou and Soong, 1985)
Reaction enthalpy ( $\Delta H_r$ )	-57.8	$\text{kJ} \cdot \text{mol}^{-1}$	(Suzuki et al., 2018)
Temperature dependency coefficient of parameter $\alpha$ of the Fujita-Doolittle equation ( $\alpha_T$ )	$8.21 \cdot 10^{-6}$	$\text{K}^{-2}$	(Chiu et al., 1983)
Termination step activation energy ( $E_t$ )	2.944	$\text{kJ} \cdot \text{mol}^{-1}$	(Baillagou and Soong, 1985)
Termination step gel and glass effect activation energy ( $E_{tr}$ )	145.84	$\text{kJ} \cdot \text{mol}^{-1}$	(Baillagou and Soong, 1985)
Termination step gel and glass effect pre-exponential factor ( $\Lambda_{tr}$ )	$1.4540 \cdot 10^{20}$	$\text{s}^{-1}$	(Baillagou and Soong, 1985)
Termination step pre-exponential factor ( $\Lambda_t$ )	$9.8000 \cdot 10^4$	$\text{m}^3 \cdot \text{mol}^{-1} \cdot \text{s}^{-1}$	(Baillagou and Soong, 1985)

### 3. Results and Discussion

#### 3.1. Batch mode operation

In a first step, the proposed model was validated against experimental data and a literature batch-mode model. In order to perform this validation, the system was simulated operating in batch mode (i.e. monomer initial load = monomer total load, monomer flow rate = 0 kg·hr<sup>-1</sup>), at 70°C and initially loaded with 300.00 kg (67.78 wt% of the initial load) of monomer (methyl methacrylate, MMA), 141.75 kg (32.06 wt% of the initial load) of solvent (benzene) and 0.86 kg (0.19 wt % of the initial load) of initiator (benzoyl peroxide, BPO). Fig. 2 compares the simulation results obtained using the model presented in this work, with the simulation results obtained using the batch-mode model proposed by Chiu and coworkers (Chiu et al., 1983), and with the experimental results obtained by Marten and Hamielec (Marten and Hamielec, 1979).

The simulated time evolution of the monomer conversion (Fig. 2.a) displays an increasing sigmoid shape: initially, the monomer conversion increases linearly with time, and then suddenly, the conversion's increase rate accelerates dramatically (i.e. autoacceleration phenomenon), to finally plateau towards the full conversion of the monomer load. The predictions of this work's model match perfectly the experimental data, and the predictions of Chiu's batch-mode model (Chiu et al., 1983).

Regarding the evolution of the average molecular weights with the monomer conversion (Fig. 2.b), the model simulation predicts an increase of the average molecular weights with the conversion, at low conversions; followed by a decrease at high conversions. The simulation results of this work's model, which reproduce very closely the simulation results of Chiu's model (Chiu et al., 1983), are in good agreement with the experimental data, especially for the number-average molecular weight.

Both, the propagation and the termination, kinetic constants decrease with the conversion (Fig. 2.c), on account of the increase of the viscosity of the reaction medium as the conversion increases (i.e. as large polymer molecules are produced). On the one hand, the termination kinetic constant starts decreasing at relatively low conversions (i.e. around 30 %), since at these conversion values the viscosity of the medium has already increased enough to hinder the mobility of large molecules (i.e. live and dead polymers), but not enough to affect the mobility of small molecules (i.e. monomers). On the other hand, the propagation kinetic constant remains unchanged until much higher conversions (i.e. around 70 %), after which it starts decreasing as well. At these higher conversions, the viscosity of the medium has increased enough to also hinder the mobility of small molecules. The kinetic constant values predicted by the model presented here, match very closely the predictions of Chiu's model (Chiu et al., 1983).

#### 3.2. Semi-batch mode operation

##### 3.2.1. Reactor dynamics

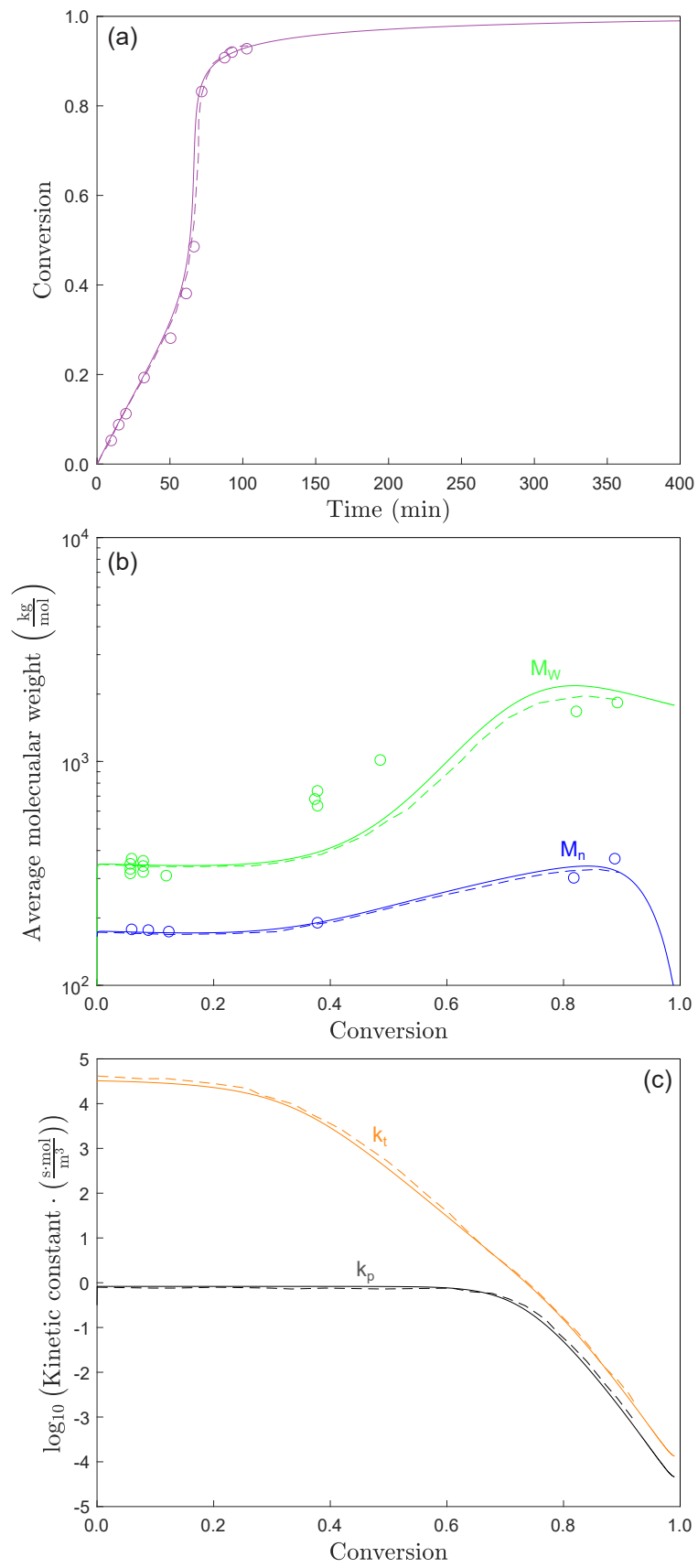
In a second step, the proposed model was used to study the one-by-one effect of four operation conditions (the input flow rate, the initiator's initial load, the temperature, and the monomer initial load) on the dynamics of the system (i.e. time evolution of the conversion, the number-average molecular weight, the thermal power, and the molar-mass dispersity).

**3.2.1.1. Input flow rate effect.** The system was simulated operating in semi-batch mode at 70°C, initially loaded with 75.0 kg (67.02 wt% of the initial load) of monomer (MMA), 35.4 kg (31.64 wt% of the initial load) of solvent (benzene) and 1.5 kg (1.34 wt% of the initial load) of initiator (BPO). During the feeding phase, the feed stream, containing monomer (600.0 kg·m<sup>-3</sup>) and solvent (276.4 kg·m<sup>-3</sup>), was fed at a

constant flow rate, until a total mass (including the initial load) of 300.00 kg of monomer was added to the reactor. The system was simulated for five different flow rates (50, 100, 150, 200 and 250 L·hr<sup>-1</sup>).

The monomer conversion increases monotonically with time (Fig. 3.a): after a first fast increase, an inflection point is reached, after which the conversion change rate increases even further, due to the gel effect (autoacceleration phenomenon). After the autoacceleration raise, the conversion change slows down, nearly plateauing; until the end of the feeding phase (i.e. when all the monomer has been introduced into the reactor), when the conversion displays a first order dynamic, tending asymptotically to full conversion (i.e. to 1.0). The feed flow rate has no effect on the first quick increase, and only has a little effect on the autoacceleration raise: the autoacceleration raise starts before (i.e. inflection point at lower times) and plateaus at higher conversion values, for lower feed flow rates. Moreover, the slope change at the inflection point is higher for higher flow rates. These trends are due to the dilution effect of the monomer flow rate: for higher monomer feed flow rates, the dilution of the reaction mixture is higher, which has two effects. On the one hand, a higher dilution leads to lower initiator concentrations, which reduces in turn the initiation reaction rate (i.e. fewer new polymer chains are produced). On the other hand, higher dilutions avoid the viscosity increase for longer times, which delays the onset of the autoacceleration phenomenon (i.e. inflection point at higher times). But once the autoacceleration starts, the monomer inventory in the reactor is higher, which results in a higher acceleration of the reaction (i.e. larger slope change at the inflection point). The monomer flow rate also affects the first-order-like final conversion increase: for higher monomer flow rates, the first-order behavior starts at lower times and displays a faster response (i.e. lower time constant). As stated previously, the final first order behavior appears when all the monomer has been introduced in the reactor, on account of the fading of the dilution effect (when no more monomer is fed into the reactor). Since the total and the initial monomer loads are the same in all the considered simulations, a higher monomer flow rate results in a shorter feeding phase; which explains why the first-order-like behavior appears before (i.e. at lower times) for higher monomer flow rates. The monomer inventory in the reactor at the end of the feeding phase is higher for higher feeding flow rates, which explains why the final first order behavior is faster for higher flow rates.

The number-average molecular weight initially increases with time, until the autoacceleration raise, when it reaches a maximum value, and starts decreasing with time (Fig. 3.b). Before the autoacceleration onset, the viscosity of the mixture is low, so the propagation reactions can take place with no hindering: the polymers grow, and therefore the average molecular weight increases with time. Once the viscosity starts increasing (during the autoacceleration raise), it starts hindering the movement of the big polymer chains, favoring the growth of the shorter chains to the detriment of the longer ones, which results in the decrease of the average molecular weight. When all the monomer has been introduced into the reactor (i.e. end of the feeding phase), the rate of decrease of the average molecular weight increases. The monomer flow rate has a significant effect on the time evolution of the average molecular weight: at higher flow rates the average molecular weight peak is higher (i.e. higher maximum average molecular weight) and is attained at longer times (i.e. peak displaced towards larger times). Higher flow rates lead to lower initiation reaction rates (see above), and therefore, when working at higher flow rates the number of new live polymers is lower, which favors the growth of existing live chains to the detriment of the formation of new ones. Moreover, higher flow rates delay the onset of the gel effect (Fig. 3.a), and therefore, the inhibition of the propagation step is also delayed. Consequently, for higher flow rates, the polymer chains can grow more before the viscosity increase hinders the propagation process, leading to larger maximum average molecular weights (i.e. higher peak). Furthermore, since the average molecular weight peaks when the gel effect becomes significant, a delay in its onset causes the average weight peak to appear after (i.e. peak displaced



(caption on next page)

**Fig. 2.** Simulation of the polymerization reactor operated in batch mode at 70°C, initially loaded with 300.00 kg of monomer (methyl methacrylate, MMA), 141.75 kg of solvent (benzene) and 0.86 kg of initiator (benzoyl peroxide, BPO). (a) Time evolution of the monomer conversion. (b) Average molecular weights ( $M_n$ : number-average;  $M_w$ : weight-average) as a function of the monomer conversion. (c) Rate constants ( $k_p$ : propagation;  $k_t$ : termination) as a function of the monomer conversion. The continuous lines represent the simulation results obtained with the model developed in this work; the dotted lines, the simulation results obtained by Chiu and coworkers (Chiu et al., 1983); and the dots, the experimental points obtained by Marten and Hamielec (Marten and Hamielec, 1979).

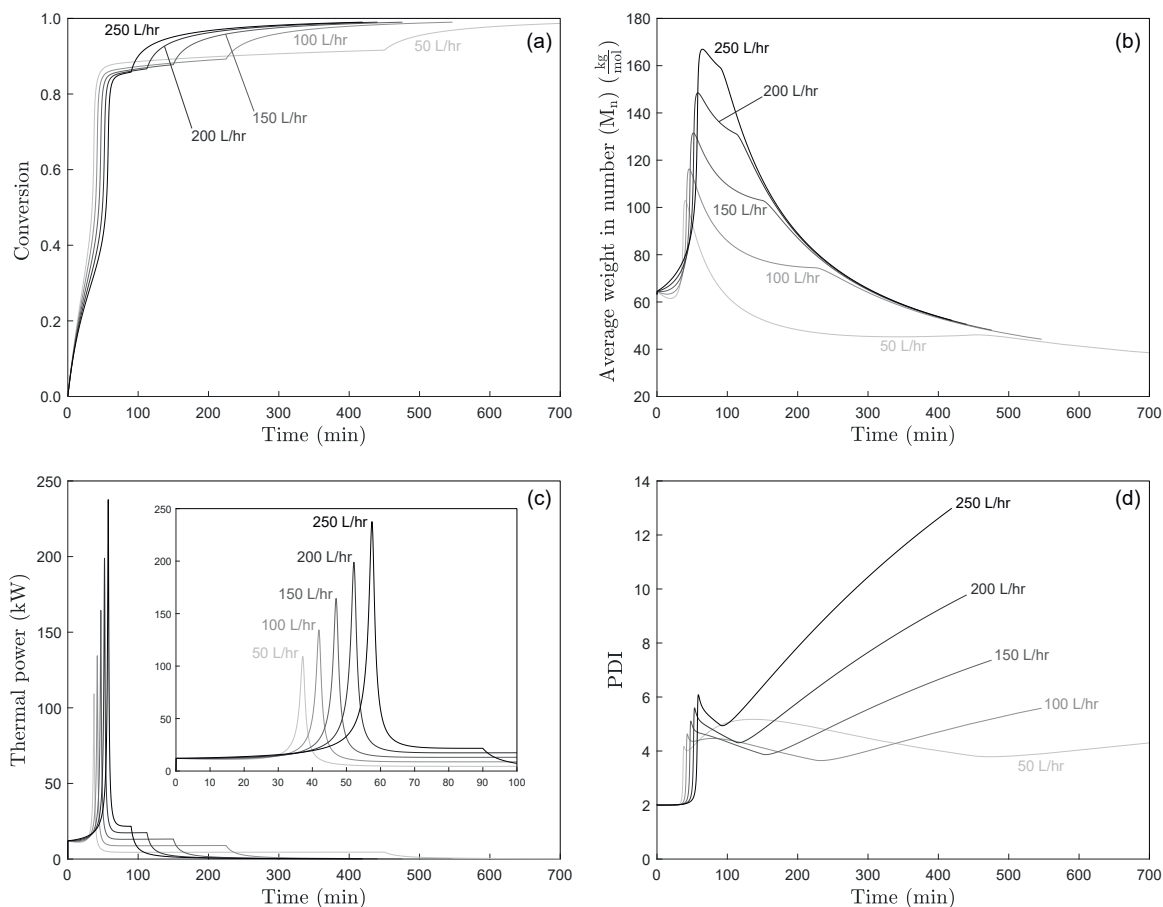


**Fig. 3.** Effect of the feeding flow rate on the time evolution of (a) the monomer conversion, (b) the number-average molecular weight, (c) the generated thermal power, and (d) the molar-mass dispersity. The reactor was simulated operating in semi-batch mode at 70°C, initially loaded with 75.0 kg of monomer (methyl methacrylate, MMA), 35.4 kg of solvent (benzene) and 1.5 kg of initiator (benzoyl peroxide, BPO). During the feeding phase, the feed stream, containing monomer ( $600.0 \text{ kg}\cdot\text{m}^{-3}$ ) and solvent ( $276.4 \text{ kg}\cdot\text{m}^{-3}$ ), was fed at a constant flow rate (50, 100, 150, 200 and  $250 \text{ L}\cdot\text{hr}^{-1}$ ), until a total mass (including the initial load) of 300.00 kg of monomer was added to the reactor.

towards larger times).

The molar-mass dispersity initially remains constant with time, until the autoacceleration raise, when it increases suddenly to reach a maximum after which it starts decreasing with time (Fig. 3.d). Before the onset of the gel effect, the propagation step is not hindered, and therefore the growth of the polymer chains is independent of their size: all the polymer chains grow at approximately the same rate, and therefore the width of the polymer size distribution does not change with time (i.e. constant molar-mass dispersity). On the contrary, once the viscosity increases and starts hindering the movement of the long polymer chains, the chain growth rate starts depending on the size of the chain, which leads to a polymer size distribution which width increases over time (i.e. increasing molar-mass dispersity). After the autoacceleration raise, the initiator's concentration in the reactor is low, which favors the propagation step to the detriment of the initiation step. Consequently, the rate of production of new polymers is neglectable after the autoacceleration raise, and nearly all the monomer is consumed to elongate already existing chains. Moreover, the growth of smaller chains is faster than the growth of larger ones, due to the mobility hindrance of the large

polymers because of the increase in the viscosity. The combination of these two phenomena causes a narrowing of the polymer size distribution (i.e. a decrease of the molar-mass dispersity). When all the monomer has been introduced into the reactor (i.e. end of the feeding phase), the molar-mass dispersity starts increasing again. After stopping the monomer feed, the monomer concentration in the reactor starts decreasing, and additionally, the viscosity of the mixture is so high that even the monomer's movement is hindered (glass effect). These effects result in a widening of the polymer size distribution (i.e. an increase of the molar-mass dispersity). The monomer flow rate has a significant effect on the time evolution of the molar-mass dispersity: higher flow rates lead to higher dispersity peaks that are attained after (i.e. at longer times). As stated previously, the dispersity's peak is associated with the gel effect onset: higher flow rates delay the onset of the gel effect (Fig. 3. a), which explains why the dispersity's peak is delayed for higher monomer flow rates. Furthermore, the autoacceleration phenomenon is more intense for higher flow rates, leading to higher dispersity peaks. Finally, the final increase in dispersity starts sooner (i.e. lower times) as the flow rate increases, since this final increase occurs at the end of the

feeding phase (which becomes shorter as the flow rate is increased).

Regarding the generated thermal power (i.e. the thermal power removed by the refrigeration system to maintain the reactor's isothermality), it initially remains constant with time, until the autoacceleration raise, when a generation peak is observed, after which the thermal power generation plateaus (Fig. 3.c). When all the monomer has been introduced into the reactor (i.e. end of the feeding phase), the generated thermal power fades out with a first-order-like response. The generation peak is generated by the autoacceleration itself: during the autoacceleration raise, the reaction rates increase sharply, leading to a sharp increase in the heat generated by the reactions. As soon as the autoacceleration raise is over, the reaction rates decrease as fast as they increased during the raise, causing the thermal power to decrease quickly as well. After the power peak, the constant feed of monomer to the reactor, maintains the reaction rates in a nearly constant residual level, which result in the (non-zero) power plateau. However, at the end of the feeding phase, the monomer starts depleting as no more monomer is added to the reactor. The monomer depletion leads to reaction fade off, resulting in the first-order-like final decrease of the generated thermal power (until it becomes 0). The monomer flow rate has a significant effect on the time evolution of the generated thermal power. On the one hand, higher flow rates lead to higher generated power peaks (i.e. higher maximum generated thermal power), which happen later (i.e. at larger times). Both trends are explained by the effect of the monomer flow rate on the autoacceleration onset (see before). On the other hand, the residual generated power after the peak is higher as the monomer flow rate increases. Higher monomer flow rates maintain higher

monomer concentration in the reactor after the acceleration rise, which result in higher residual reaction rates, and therefore in higher generated thermal powers.

**3.2.1.2. Initiator's initial load effect.** The system was simulated operating in semi-batch mode at 70°C, initially loaded with 75.0 kg (67.62 wt%, 67.32 wt%, 67.02 wt%, 66.73 wt%, and 66.43 wt% of the initial load, for the different initiator initial loads) of monomer (MMA), 35.4 kg (31.92 wt%, 31.78 wt%, 31.64 wt%, 31.49 wt%, and 31.35 wt% of the initial load, for the different initiator initial loads) of solvent (benzene) and an initial load of initiator (BPO). During the feeding phase, the feed stream, containing monomer ( $600.0 \text{ kg}\cdot\text{m}^{-3}$ ) and solvent ( $276.4 \text{ kg}\cdot\text{m}^{-3}$ ), was fed at a constant flow rate of  $150 \text{ L}\cdot\text{hr}^{-1}$ , until a total mass (including the initial load) of 300.00 kg of monomer was added to the reactor. The system was simulated for five different initiator initial loads 0.5 kg (0.45 wt% of the initial load), 1.0 kg (0.90 wt% of the initial load), 1.5 kg (1.34 wt% of the initial load), 2.0 kg (1.78 wt% of the initial load) and 2.5 kg (2.21 wt% of the initial load).

The initiator load has a significant effect on the autoacceleration raise of the time evolution of the monomer conversion (i.e. first part of the curve of Fig. 4.a). On the contrary, it does not have any effect neither on the conversion value of the plateau after the raise (i.e. the conversion reached after the autoacceleration raise is the same for all the initiator loads), nor on the first-order-like final conversion increase (Fig. 4.a). The initial slope of the conversion curve is lower for lower initiator loads; but at the inflection point, the slope change is higher. Moreover, the autoacceleration raise starts after (i.e. inflection point at higher times)

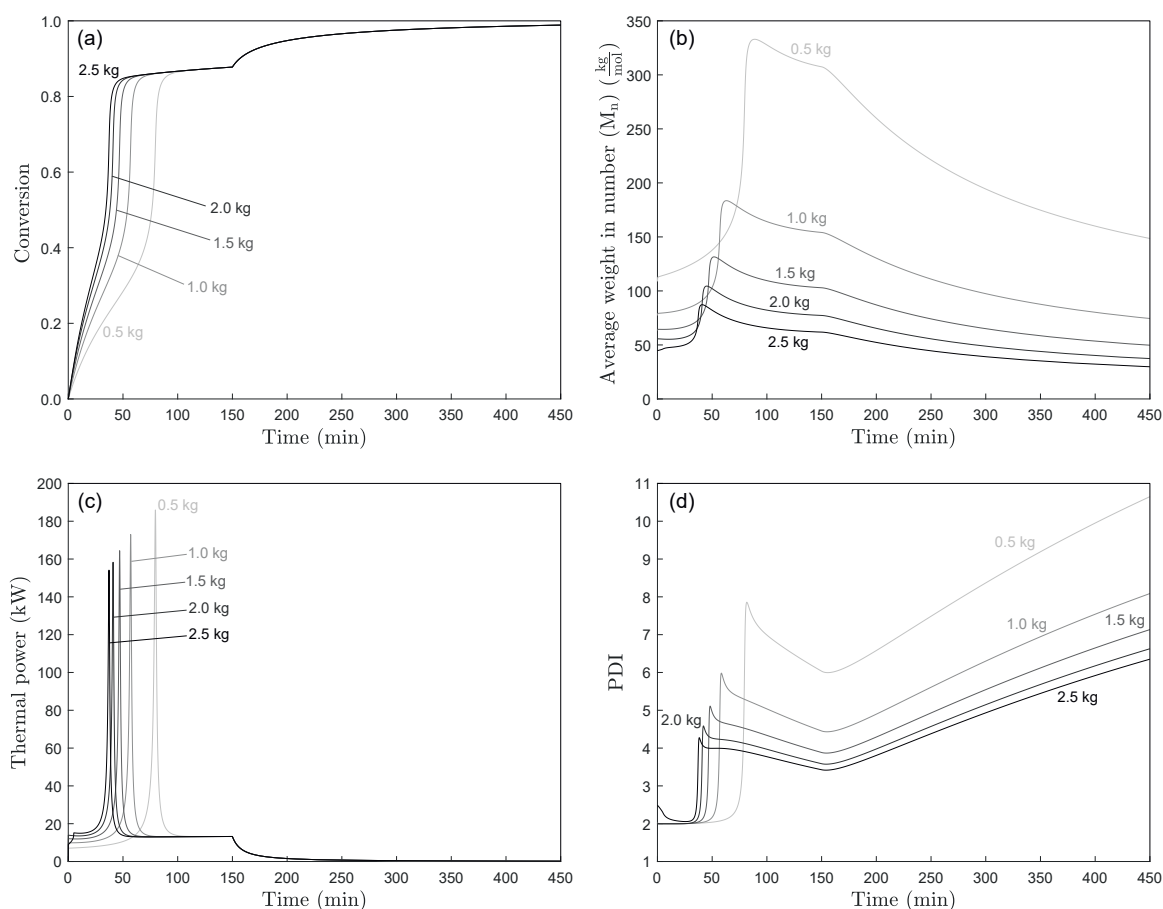


**Fig. 4.** Effect of the initiator load on the time evolution of (a) the monomer conversion, (b) the number-average molecular weight, (c) the generated thermal power, and (d) the molar-mass dispersity. The reactor was simulated operating in semi-batch mode at 70°C, initially loaded with 75.0 kg of monomer (methyl methacrylate, MMA), 35.4 kg of solvent (benzene) and the load (0.5, 1.0, 1.5, 2.0 and 2.5 kg) of initiator (benzoyl peroxide, BPO). During the feeding phase, the feed stream, containing monomer ( $600.0 \text{ kg}\cdot\text{m}^{-3}$ ) and solvent ( $276.4 \text{ kg}\cdot\text{m}^{-3}$ ), was fed at a constant flow rate of  $150 \text{ L}\cdot\text{hr}^{-1}$ , until a total mass (including the initial load) of 300.00 kg of monomer was added to the reactor.

for lower initiator loads. Lower initiator loads (with the same monomer and solvent initial load, and the same feed flow rate) result in lower initiator concentrations in the reaction mixture. Lower initiator concentrations lead to lower initiation reaction rates, and therefore to lower inventories of live chains (i.e. fewer new chains are produced per unit time). In turn, lower inventories of growing polymers limit all the subsequent reactions, limiting the monomer consumption and resulting in a lower initial slope of the time evolution of the conversion. However, a lower monomer consumption leads to higher monomer inventories, since the monomer input is constant (i.e. same monomer initial load, and same feed flow rate). Consequently, a lower initiator load causes a higher monomer inventory at the moment of the autoacceleration onset, which results in a higher acceleration of the reaction (i.e. larger slope change at the inflection point). The initiator load has no effect on the last part of the conversion curve since this part of the curve is associated with the fading of the dilution effect when the monomer feed is stopped at the end of the feeding phase (see Section 3.2.1.1.), and the initiator load has no effect on it.

The time evolution of the number-average molecular weight is strongly affected by the initiator initial load (Fig. 4.b): lower loads lead to higher average molecular weight peaks (i.e. higher maximum average molecular weights) that are reached at longer times (i.e. peak displaced towards larger times). As explained before, lower initiator loads lead to lower inventories of growing polymers, which favors the growth of existing live chains to the detriment of the formation of new ones, resulting in a size distribution with a higher average molecular weight. Since the average weight peak is associated with the autoacceleration raise, its displacement towards later times when lower initiator loads are used, is due to the later onset of the autoacceleration (see above).

Lower initiator loads displace the molar-mass dispersity peak towards later times, and increase the peak height (Fig. 4.d). Since the dispersity's peak is associated with the autoacceleration onset (see Section 3.2.1.1.), the effect of the initiator load on the peak is explained by the effect of the initiator load on the autoacceleration raise (Fig. 4.a).

Finally, the initiator load also has a significant effect on the thermal power generation (Fig. 4.c). Firstly, the initial power plateau (before the peak) is displaced towards lower power values for lower initiator loads. This trend arises from the fact that lower initiator loads lead to lower reaction rates before the autoacceleration raise (lower initial slopes in Fig. 4.a), and consequently lower thermal power generation. Secondly, the generation peak is higher and happens at later times for lower initiator loads. The thermal power generation peak is generated by the autoacceleration raise, which occurs at later times for lower initiator loads (Fig. 4.a). As explained previously, a lower initiator load results in a more severe reaction acceleration during the autoacceleration raise, which in turn generates a higher generation peak. Lastly, the residual generation plateau (i.e. after the generation peak) and the final first-order-like power fading are unaffected by the initiator load. As explained in Section 3.2.1.1., the final features of the time evolution curves of the generated power are mainly associated to the monomer concentration in the reactor after the autoacceleration raise. The initiator load has no effect on the latter concentration, and therefore, it does not change the residual power generation and the final generation fading.

**3.2.1.3. Temperature effect.** The system was simulated operating in semi-batch mode at a constant temperature, initially loaded with 75.0 kg (67.02 wt% of the initial load) of monomer (MMA), 35.4 kg (31.64 wt% of the initial load) of solvent (benzene) and 1.5 kg (1.34 wt % of the initial load) of initiator (BPO). During the feeding phase, the feed stream, containing monomer ( $600.0 \text{ kg}\cdot\text{m}^{-3}$ ) and solvent ( $276.4 \text{ kg}\cdot\text{m}^{-3}$ ), was fed at a constant flow rate of  $150 \text{ L}\cdot\text{hr}^{-1}$ , until a total mass (including the initial load) of 300.00 kg of monomer was added to the reactor. The system was simulated for five different operation temperatures (60°C, 65°C, 70°C, 75°C, and 80°C).

The reactor temperature has a strong effect on the reactor dynamics (i.e. time evolution of the monomer conversion). Firstly, the initial slope of the conversion curve is lower for lower temperatures (Fig. 5.a). Secondly, at lower temperatures the autoacceleration raise starts after (i.e. inflection point at higher times), and the acceleration is less dramatic (i.e. lower increase of the slope at the inflection point). Furthermore, after the acceleration raise, the conversion plateaus at lower conversion values for lower reactor temperatures (Fig. 5.a). Lastly, the first-order-like final conversion increase starts at the same time for all the temperatures, and displays approximately the same time constant. Higher reactor temperatures accelerate all the reactions (Arrhenius-like kinetic constant increase) and the transport of the different compounds. For a given reactor initial composition and monomer feeding rate, the increase in the temperature results in an increase of the reaction rates, which in turn lead to faster monomer conversion (i.e. higher initial slope of the conversion curve), and a more severe autoacceleration raise (i.e. higher increase of the slope at the inflection point, and a higher conversion plateau after the raise).

The reactor temperature also has an important effect on the time evolution of the number-average molecular weight (Fig. 5.b): lower reactor temperatures lead to higher average molecular weight peaks (i.e. higher maximum average molecular weights) that are reached at longer times (i.e. peak displaced towards larger times) and are wider. Moreover, the number-average molecular weight decreases more after the peak for lower temperatures. For instance, at 60°C, the maximum number-average molecular weight is around  $345 \text{ kg}\cdot\text{mol}^{-1}$  and, at the end of the polymerization, the average molecular weight is around  $250 \text{ kg}\cdot\text{mol}^{-1}$  (~28 % decrease); whereas at 80°C, the maximum number-average molecular weight is around  $50 \text{ kg}\cdot\text{mol}^{-1}$  and, at the end of the polymerization, the average molecular weight is around  $45 \text{ kg}\cdot\text{mol}^{-1}$  (~10 % decrease). Since the average weight peak is associated with the autoacceleration raise, its displacement towards later times at lower temperatures, is due to the later onset of the autoacceleration at these temperatures (see above). In the 60°C to 80°C temperature range, the increase of the termination kinetic constant with temperature is significantly higher than the increase of the propagation kinetic constant. Consequently, at lower reactor temperatures (in the 60°C to 80°C range), the propagation-termination ratio is higher, which leads to longer polymers (i.e. higher average molecular weights) since a given chain has more probability to grow than to terminate. The number-average molecular weight decrease after the peak is related to the viscosity increase of the gel effect (see Section 3.2.1.1.). Since lower temperatures lead to longer polymer chains, the increase in viscosity is higher at lower reactor temperatures, and therefore, the gel effect is more severe at these temperatures. The effect of the temperature on the severity of the gel effect explains why for lower temperatures, the number-average molecular weight decreases more after the peak.

The temperature has a strong effect on the time evolution curves of the molar-mass dispersity (Fig. 5.d). The shape of the curves for 60°C, 65°C, and 70°C, is the one described in Section 3.2.1.1.; whereas, the initial part of the curves for 75°C and 80°C is significantly different: instead of an initial constant dispersity (until the autoacceleration peak), at these temperatures, the dispersity decreases initially. Moreover, the initial molar-mass dispersity is 2.0 for 60°C, 65°C, and 70°C; and is substantially higher for 75°C and 80°C (2.9 and 5.4, respectively). A molar-mass dispersity value of 2 is consistent with an exclusive termination by disproportionation (reaction R5) (Marien et al., 2021). At higher temperatures, the initiation and activation reactions are over boosted, which generates a wider initial size distribution (i.e. higher initial molar-mass dispersities). Lower temperatures make the molar-mass dispersity peak to happen at later times, and with greater increases at the peak (i.e. larger difference between the dispersity peak value and the value before the onset of the autoacceleration). These trends arise from the effect of the temperature on the reaction rates: lower temperatures decrease the reaction rates, which lead to a longer autoacceleration raise (Fig. 5.a). The dispersity increase during longer

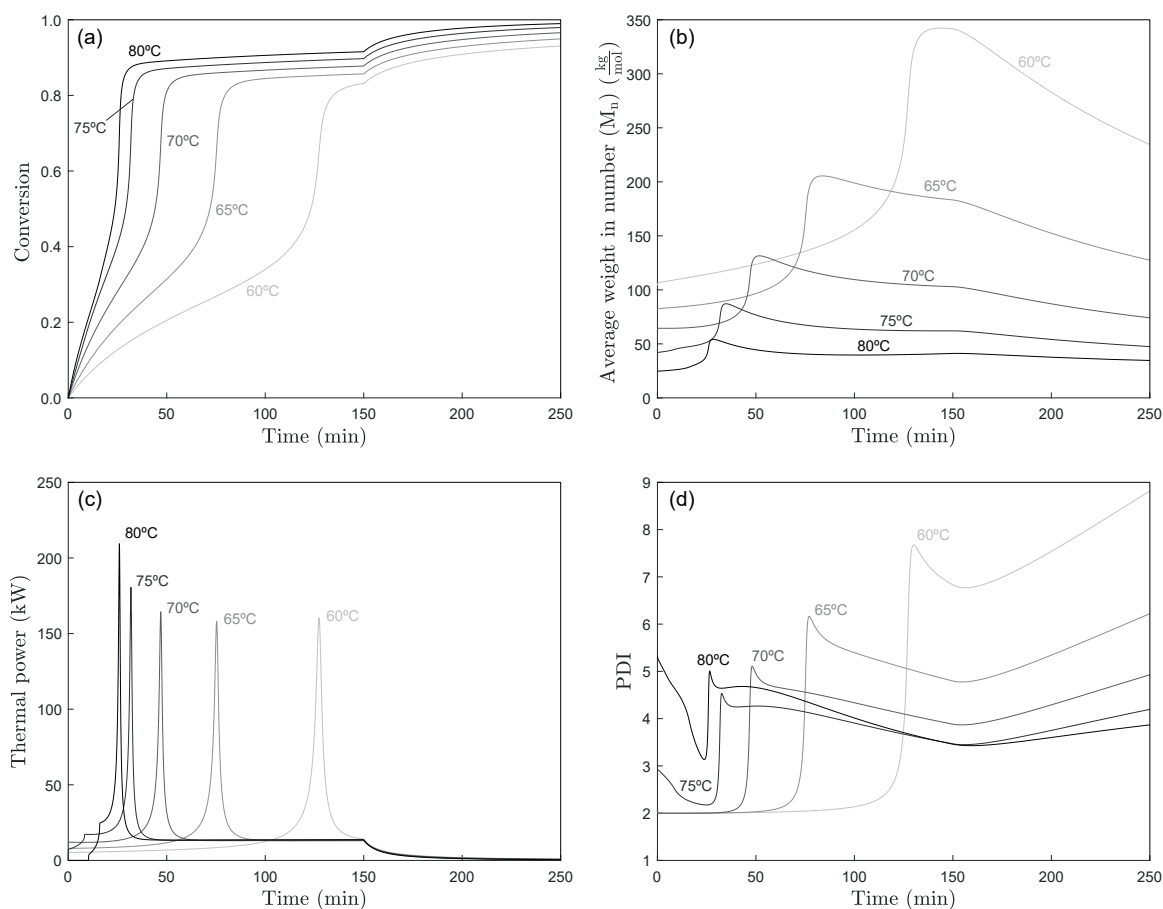


**Fig. 5.** Effect of the reactor temperature on the time evolution of (a) the monomer conversion, (b) the number-average molecular weight, (c) the generated thermal power, and (d) the molar-mass dispersity. The reactor was simulated operating in semi-batch mode at constant temperature (60°C, 65°C, 70°C, 75°C, and 80°C), initially loaded with 75.0 kg of monomer (methyl methacrylate, MMA), 35.4 kg of solvent (benzene) and 1.5 kg of initiator (benzoyl peroxide, BPO). During the feeding phase, the feed stream, containing monomer ( $600.0 \text{ kg}\cdot\text{m}^{-3}$ ) and solvent ( $276.4 \text{ kg}\cdot\text{m}^{-3}$ ), was fed at a constant flow rate of  $150 \text{ L}\cdot\text{hr}^{-1}$ , until a total mass (including the initial load) of 300.00 kg of monomer was added to the reactor.

autoacceleration raises is higher, which explains why the dispersity increase at the peak is larger at lower temperatures.

Finally, the thermal power generation is also significantly affected by the reactor temperature (Fig. 5.c). For 60°C, 65°C, and 70°C, the thermal power generation curve presents the same shape described in Section 3.2.1.1. However, for 75°C and 80°C, the initial part of the curve is different: instead of starting with a power plateau, the generated power is initially negligible and ramps up exponentially until it plateaus, before the generation peak. Firstly, the initial power plateau (before the peak) is displaced towards lower power values for lower temperatures. This trend arises from the fact that lower temperatures lead to lower reaction rates before the autoacceleration raise (lower initial slopes in Fig. 5.a), and consequently lower thermal power generation. Secondly, the generation peak is lower, wider, and happens at later times for lower temperatures. The thermal power generation peak is generated by the autoacceleration raise, which occurs at later times for lower temperatures (Fig. 5.a). Moreover, lower temperatures decrease the reaction rates, which causes that the acceleration raise is less severe and lasts longer times (i.e. the slope of the conversion curve after the inflection point is lower, and the time from the onset of the autoacceleration until the conversion plateau is longer). The combination of both factors leads to a lower and wider power generation peak. Lastly, the residual generation plateau (i.e. after the generation peak) and the final first-order-like power fading are unaffected by the temperature.

**3.2.1.4. Monomer initial load effect.** The system was simulated operating in semi-batch mode at 70°C, initially loaded with an initial load of

monomer (MMA) and solvent (benzene), and 1.5 kg (1.68 wt%, 0.85 wt%, 0.57 wt%, 0.43 wt%, and 0.34 wt% of the initial load, for the different monomer initial loads) of initiator (BPO). During the feeding phase, the feed stream, containing monomer ( $600.0 \text{ kg}\cdot\text{m}^{-3}$ ) and solvent ( $276.4 \text{ kg}\cdot\text{m}^{-3}$ ), was fed at a constant flow rate of  $150 \text{ L}\cdot\text{hr}^{-1}$ , until a total mass (including the initial load) of 300.00 kg of monomer was added to the reactor. The system was simulated for five different monomer initial loads (20, 40, 60, 80 and 100 % of the total load).

The monomer initial load changes substantially the conversion curve (Fig. 6.a). The initial slope of the conversion curve is higher for lower monomer initial loads; but at the inflection point, the slope change is lower. Moreover, the autoacceleration raise starts before (i.e. inflection point at lower times) for lower monomer initial loads. Lower monomer initial loads (with the same initiator initial load, and the same feed rate) result in higher initiator concentrations in the reaction mixture, which explain the trends observed in the initial part of the conversion curves with the initial monomer load (see Section 3.2.1.2.). The monomer initial load also has a slight effect on the conversion plateau after the autoacceleration raise (Fig. 6.a): for lower monomer initial loads, the conversion plateaus at slightly lower conversions. Finally, the first-order-like final conversion increase starts later for lower monomer initial loads. This feature is associated with the moment when all the monomer has been introduced in the reactor (see Section 3.2.1.1.). Since the total monomer load and the feed rates are the same in all the considered simulations, a lower monomer initial load results in a longer feeding phase; which explains why the first-order-like behavior appears later (i.e. at higher times) for lower monomer initial loads. The limit

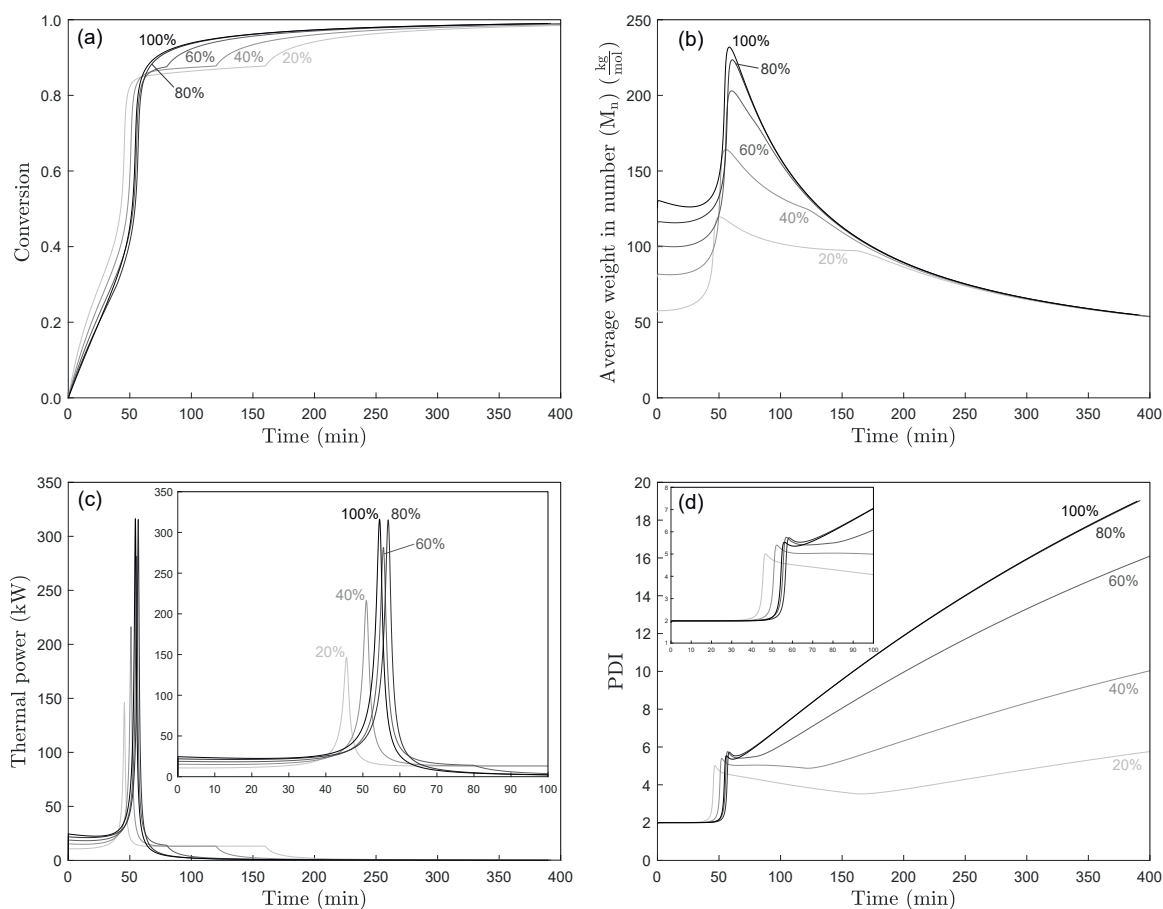


**Fig. 6.** Effect of the monomer initial load on the time evolution of (a) the monomer conversion, (b) the number-average molecular weight, (c) the generated thermal power, and (d) the molar-mass dispersity. The reactor was simulated operating in semi-batch mode at 70°C, initially loaded with an initial load (20, 40, 60, 80 and 100 % of the total load) of monomer (methyl methacrylate, MMA) and solvent (benzene), and 1.5 kg of initiator (benzoyl peroxide, BPO). During the feeding phase, the feed stream, containing monomer ( $600.0 \text{ kg}\cdot\text{m}^{-3}$ ) and solvent ( $276.4 \text{ kg}\cdot\text{m}^{-3}$ ), was fed at a constant flow rate of  $150 \text{ L}\cdot\text{hr}^{-1}$ , until a total mass (including the initial load) of  $300.00 \text{ kg}$  of monomer was added to the reactor.

case, 100 % monomer initial load (i.e. operation in batch mode), does not present the intermediate conversion plateau: after the autoacceleration raise, the conversion tends directly asymptotically to full conversion.

The monomer initial load also has a strong effect on the number-average molecular weight curve (Fig. 6.b): lower monomer initial loads lead to lower average molecular weight peaks (i.e. lower maximum average molecular weights) that are reached before (i.e. peak displaced towards lower times). Since the average weight peak is associated with the autoacceleration raise, its displacement towards later times when higher initiator loads are used, is due to the later onset of the autoacceleration for higher monomer initial loads (Fig. 6.a). As stated before, lower monomer initial loads result in higher initiator concentrations in the reaction mixture, which explains why lower monomer initial loads lead to lower maximum average molecular weight (see Section 3.2.1.2.).

For monomer initial loads between 20 % and 80 %, higher values move the molar-mass dispersity peak towards later times, and increase the peak height (Fig. 6.d). This is consistent with the fact that higher monomer initial loads lead to lower initiator concentrations in the reaction mixture (see Section 3.2.1.2.). However, the 100 % curve (i.e. operation in batch mode) breaks the trend, displaying an intermediate dispersity peak at an intermediate time (i.e. between the 40 % and 60 % peaks). This singularity is due to the fact that when the reactor is operated in batch mode there is no feed stream, and therefore, no dilution effect (see Section 3.2.1.1.).

Finally, the thermal power generation curve changes significantly

with the monomer initial load (Fig. 6.c). Firstly, the initial power plateau (before the peak) is displaced towards lower power values for lower monomer initial loads. Secondly, for monomer initial loads between 20 % and 80 %, the generation peak is higher and happens at later times for higher monomer initial loads. Higher monomer initial loads translate in lower initiator concentrations. As discussed in Section 3.2.1.2., lower initiator concentrations result in a more severe reaction acceleration during the autoacceleration raise, which in turn generates a higher generation peak. As in the dispersity case, the 100 % curve also breaks the trend of power generation, since the generation peak happens at times between the 40 % and 60 % generation peaks. This exception is due to the lack of dilution effect when the reactor is operated in batch mode. Lastly, the residual generation plateau (i.e. after the generation peak) is not affected by the monomer initial load, whereas the final first-order-like power fading starts at later times for lower monomer initial loads. Since the total monomer load and the feed rates are the same in all the considered simulations, a lower monomer initial load results in a longer feeding phase; which explains why the first-order-like behavior appears later (i.e. at higher times) for lower monomer initial loads.

### 3.2.2. Final product characteristics, and reactor safety and productivity

Finally, in a third step, the proposed model was used to study the combined effect of three operation conditions (the input flow rate, the initiator's initial load, and the reactor temperature) on the final product characteristics (i.e. final number-average molecular weight and final molar-mass dispersity), and the reactor safety (i.e. maximum generated

thermal power) and productivity (i.e. polymerization time). The system was simulated operating in semi-batch mode at a constant temperature, initially loaded with 75.0 kg (66.14 wt%-67.63 wt% of the initial load, depending on the initial initiator load) of monomer (MMA), 35.4 kg (31.22 wt%-31.92 wt% of the initial load, depending on the initial initiator load) of solvent (benzene) and an initial load of initiator (BPO). During the feeding phase, the feed stream, containing monomer ( $600.0 \text{ kg}\cdot\text{m}^{-3}$ ) and solvent ( $276.4 \text{ kg}\cdot\text{m}^{-3}$ ), was fed at a constant flow rate, until a total mass (including the initial load) of 300.00 kg of monomer was added to the reactor. Figs. 7, 8 and 9 present the effect of the initiator load and the feed flow rate on the final number-average molecular weight (subfigures a), the final molar-mass dispersity (subfigures b), the maximum generated thermal power (subfigures c), and the polymerization time (subfigures d), at 3 different reactor temperatures (Fig. 7: 60°C, Fig. 8: 70°C, and Fig. 9: 80°C).

For a specific reactor temperature, operating the reactor at a larger feed flow rate produces a polymer with a higher final number-average molecular weight; while using a larger initiator load produces a polymer with a lower one (Fig. 7.a, 8.a and 9.a). These trends are consistent with the results discussed in Section 3.2.1.1. and 3.2.1.2., respectively. Furthermore, for a certain feed flow rate and initiator load, operating the reactor at higher temperatures produces a polymer with a lower final number-average molecular weight (comparison between Fig. 7.a, 8.a and 9.a), which is consistent with the discussion presented in Section 3.2.1.3.

For a given reactor temperature and feed flow rate, operating the reactor with a larger initiator load produces a product with lower molar-

mass dispersity (Fig. 7.b, 8.b and 9.b), which is consistent with the discussion presented in Section 3.2.1.2. For a particular reactor temperature and initiator load, the effect of the feed flow rate on the final product's dispersity is not monotonous: for low flow rates, an increase of the flow leads to a decrease of the final dispersity; whereas for high flow rates, an increase of the flow leads to an increase of the final dispersity. These two trends generate a minimum dispersity at the turning point. The position of this minimum depends on the initiator load and the temperature. For some combinations of temperature and initiator load, the minimum is outside of the considered operation space, and therefore the effect of the feed flow rate is monotonous (as in Section 3.2.1.1.). Two opposing effects of the feed flow rate on the dispersity explain the observed behavior. On the one hand, an increase of the feed flow causes a decrease of the initiator concentration in the reactor, which lowers the dispersity. On the other hand, an increase of the feed flow causes a longer autoacceleration raise, which raises the dispersity. The balance between these two opposing effects generates the observed trends: for low feed flow rates, the first effect dominates; whereas, for high feed flow rates, the second one dominates. Furthermore, for a specific feed flow rate and initiator load, operating the reactor at higher temperatures produces a polymer with a lower final molar-mass dispersity (comparison between Fig. 7.b, 8.b and 9.b), which is consistent with the discussion presented in Section 3.2.1.3.

For a given reactor temperature, operating the reactor at a larger feed flow rate leads to a larger maximum generated thermal power; while using a larger initiator load results in a lower maximum generated thermal power (Fig. 7.c, 8.c and 9.c). The effect of the feed flow rate on

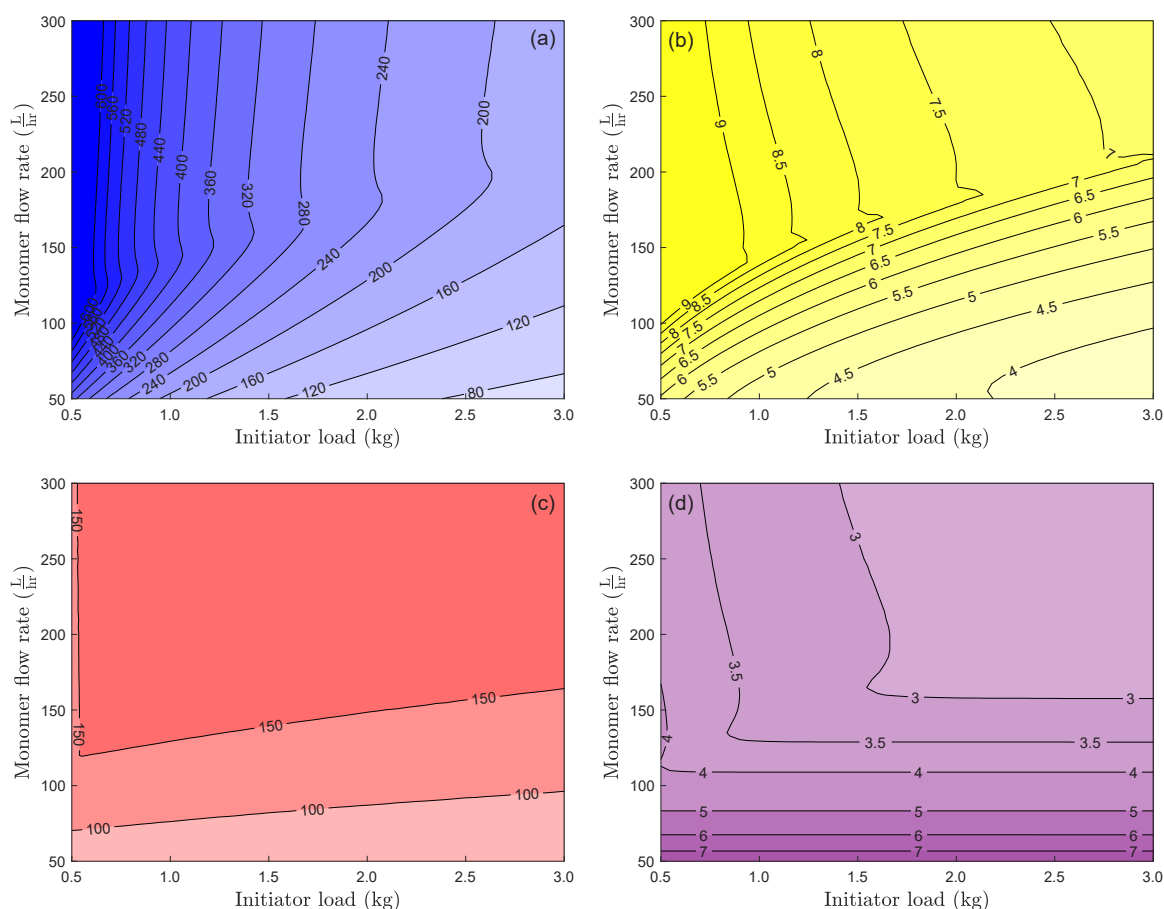


**Fig. 7.** Effect of the initiator load and the monomer flow rate on (a) the final number-average molecular weight, expressed in  $\text{kg}\cdot\text{mol}^{-1}$ ; (b) the molar-mass dispersity; (c) the maximum generated thermal power, expressed in kW; and (d) the polymerization time (time to reach a monomer conversion of 90 %), expressed in hr. The reactor was simulated operating in semi-batch mode at 60°C, initially loaded with 75.0 kg of monomer (methyl methacrylate, MMA), 35.4 kg of solvent (benzene) and the initiator (benzoyl peroxide, BPO) load. During the feeding phase, the feed stream, containing monomer ( $600.0 \text{ kg}\cdot\text{m}^{-3}$ ) and solvent ( $285.5 \text{ kg}\cdot\text{m}^{-3}$ ), was fed at a constant flow rate, until a total mass (including the initial load) of 300.00 kg of monomer was added to the reactor.

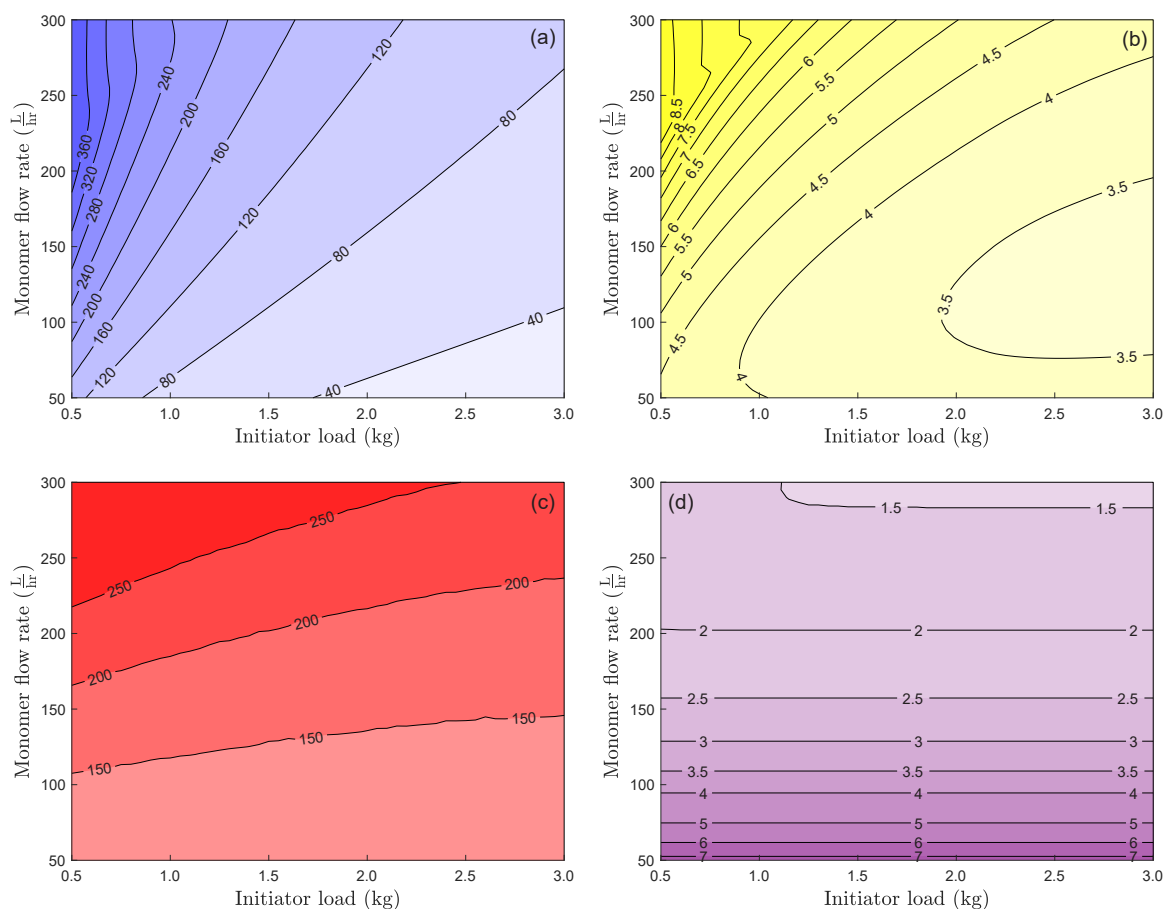


**Fig. 8.** Effect of the initiator load and the monomer flow rate on (a) the final number-average molecular weight, expressed in  $\text{kg}\cdot\text{mol}^{-1}$ ; (b) the molar-mass dispersity; (c) the maximum generated thermal power, expressed in kW; and (d) the polymerization time (time to reach a monomer conversion of 90 %), expressed in hr. The reactor was simulated operating in semi-batch mode at  $70^\circ\text{C}$ , initially loaded with 75.0 kg of monomer (methyl methacrylate, MMA), 35.4 kg of solvent (benzene) and the initiator (benzoyl peroxide, BPO) load. During the feeding phase, the feed stream, containing monomer ( $600.0\text{ kg}\cdot\text{m}^{-3}$ ) and solvent ( $285.5\text{ kg}\cdot\text{m}^{-3}$ ), was fed at a constant flow rate, until a total mass (including the initial load) of 300.00 kg of monomer was added to the reactor.

the maximum generated thermal power is substantially higher than the initiator load's one. These trends are consistent with the results discussed in Section 3.2.1.1. and 3.2.1.2., respectively. Furthermore, for a particular feed flow rate and initiator load, operating the reactor at higher temperatures generates a higher maximum thermal power peak (comparison between Fig. 7.c, 8.c and 9.c), which is consistent with the discussion presented in Section 3.2.1.3.

The polymerization time was defined in this work as the time required to achieve a 90 % global conversion, and was used as a proxy for reactor productivity. For high temperatures (i.e.  $80^\circ\text{C}$ ), the initiator load has no effect on the polymerization time, so at these temperatures, the reactor productivity only depends on the feed flow rate (Fig. 9.d): higher flow rates result in higher reactor productivities (i.e. lower polymerization times). On the contrary, for lower temperatures, the initiator load does have an effect on the polymerization time (Fig. 7.d and 8.d). For these temperatures, two different trends appear depending on the feed flow rate value. For high feed flow rates, an increase of the initiator load results in a lower polymerization time. For these high feed flow rates, the flow rate has little effect on the polymerization time, and the productivity depends nearly entirely on the initiator load. For low feed flow rates, the initiator load has no effect on the polymerization time, and the reactor productivity only depends on the feed flow rate (as at high temperatures). The feed flow rate that limits both regions moves towards higher values when the temperature increases (comparison between Fig. 7.d, 8.d and 9.d). For instance, at  $60^\circ\text{C}$ , the flow threshold is of about  $125\text{ L}\cdot\text{hr}^{-1}$  (Fig. 7.d); for  $70^\circ\text{C}$ , it is around  $275\text{ L}\cdot\text{hr}^{-1}$  (Fig. 8.d); and for  $80^\circ\text{C}$ , it is above  $300\text{ L}\cdot\text{hr}^{-1}$  (Fig. 9.

d), since the bifurcation is outside of the considered operation space. In operation conditions in which the limiting factor is the monomer feeding (i.e. low flow rates and high temperatures), the polymerization time only depends on the feed flow and does not depend on the initiator load. In these conditions, the reactor productivity can be set by adjusting the monomer feed flow. On the contrary, in operation conditions in which the limiting factor is the reaction (i.e. high flow rates and low temperatures), the polymerization time depends strongly on the initiator load and only slightly on the monomer feed flow rate.

#### 4. Conclusions

In this work, a model of a MMA solution polymerization reactor operating in semi-batch mode was developed. The model allows to simulate the time-evolution of the monomer conversion, quality characteristics of the produced polymer such as the polymer's average molecular weight and its molar-mass dispersity, and safety related parameters such as the generated thermal power. Although the developed model considers a reactor operating in semi-batch mode, it can also be used for simulating reactors operating in batch mode. The simulation results of a batch reactor with the developed model are consistent with experimental data and with other batch reactor models available in literature.

The developed model was used to study the effect of different operation conditions (feeding flow rate, initiator load, monomer initial load, and reactor temperature) on the dynamical curves of the reactor (i.e. time evolution of the monomer conversion, the average molecular

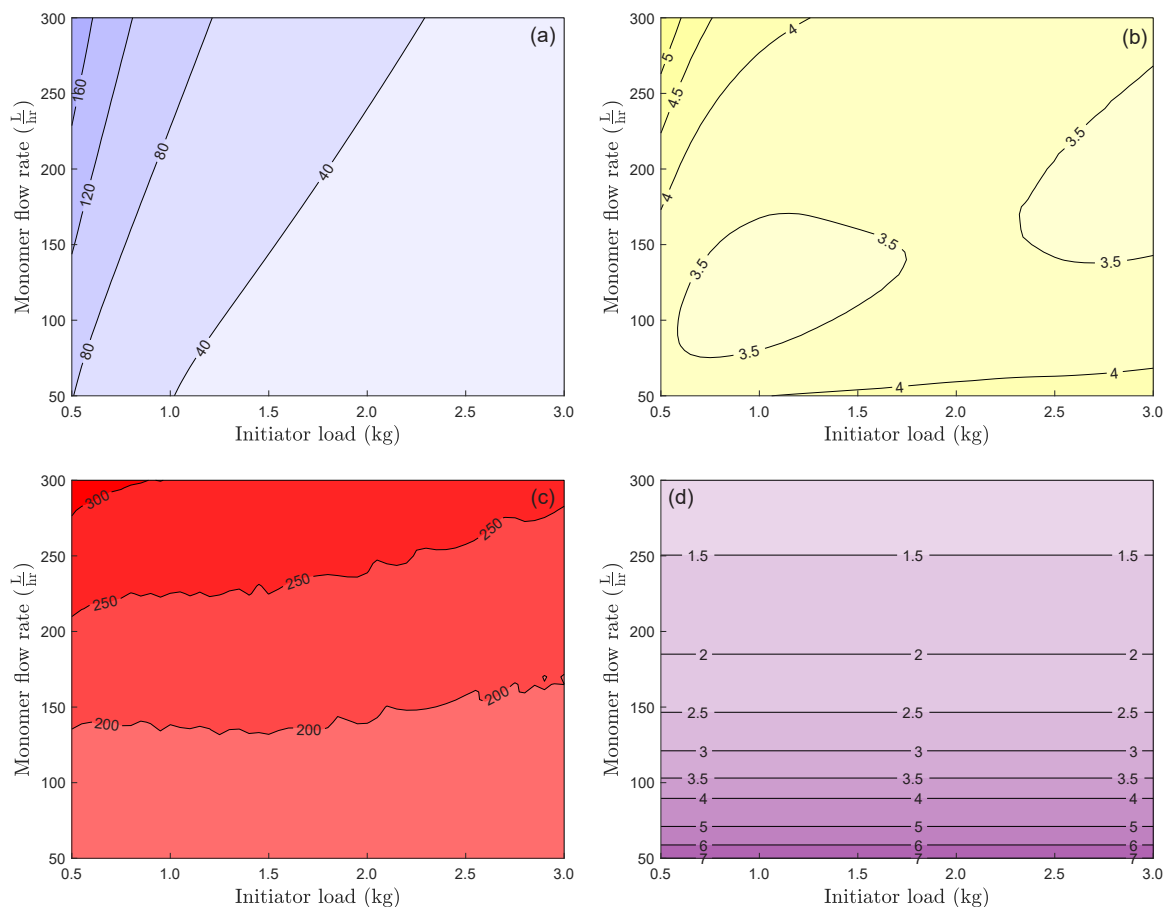


**Fig. 9.** Effect of the initiator load and the monomer flow rate on (a) the final number-average molecular weight, expressed in  $\text{kg}\cdot\text{mol}^{-1}$ ; (b) the molar-mass dispersity; (c) the maximum generated thermal power, expressed in kW; and (d) the polymerization time (time to reach a monomer conversion of 90 %), expressed in hr. The reactor was simulated operating in semi-batch mode at  $80^\circ\text{C}$ , initially loaded with 75.0 kg of monomer (methyl methacrylate, MMA), 35.4 kg of solvent (benzene) and the initiator (benzoyl peroxide, BPO) load. During the feeding phase, the feed stream, containing monomer ( $600.0 \text{ kg}\cdot\text{m}^{-3}$ ) and solvent ( $285.5 \text{ kg}\cdot\text{m}^{-3}$ ), was fed at a constant flow rate, until a total mass (including the initial load) of 300.00 kg of monomer was added to the reactor.

weight, the dispersity and the generated thermal power) when operated in semi-batch mode. Subsequently, the developed model was used to study the combined effect of three operation conditions (the input flow rate, the initiator's initial load, and the reactor temperature) on the final product characteristics (i.e. final number-average molecular weight and final molar-mass dispersity), and the reactor safety (i.e. maximum generated thermal power) and productivity (i.e. polymerization time). All the obtained results are consistent with the real behaviour of MMA solution polymerization reactors. Thus, this model can be used to optimize the operation conditions of the semi-batch reactor so that the final product quality meets the application requirements, while maintaining the reactor within its safe-operation envelope, and maximizing its productivity.

### Nomenclature

#### Roman symbols

$A$	Exchange area of the refrigeration system ( $\text{m}^2$ )
$C_{p_j}$	Mass heat capacity of stream $j$ ( $\text{J}\cdot\text{K}^{-1}\cdot\text{g}^{-1}$ )
$E_d$	Activation energy of the activation step ( $\text{J}\cdot\text{mol}^{-1}$ )
$E_i$	Activation energy of the initiation step ( $\text{J}\cdot\text{mol}^{-1}$ )
$E_p$	Activation energy of the propagation step ( $\text{J}\cdot\text{mol}^{-1}$ )
$E_{op}$	Activation energy of the gel and glass effect on the propagation step ( $\text{J}\cdot\text{mol}^{-1}$ )
$E_t$	Activation energy of the termination step ( $\text{J}\cdot\text{mol}^{-1}$ )
$E_{ot}$	Activation energy of the gel and glass effect on the termination step ( $\text{J}\cdot\text{mol}^{-1}$ )
$f$	Initiator efficiency factor
$I$	Initiator
$k_d$	Kinetic constant of the activation step ( $\text{s}^{-1}$ )
$k_i$	Kinetic constant of the initiation step ( $\text{m}^3\cdot\text{mol}^{-1}\cdot\text{s}^{-1}$ )

(continued on next column)

(continued)

$k_p$	Kinetic constant of the propagation step ( $\text{m}^3\cdot\text{mol}^{-1}\cdot\text{s}^{-1}$ )
$k_p^0$	Kinetic constant of the propagation step at zero conversion ( $\text{m}^3\cdot\text{mol}^{-1}\cdot\text{s}^{-1}$ )
$k_{op}$	Kinetic constant of the gel and glass effect on the propagation step ( $\text{s}^{-1}$ )
$k_t$	Kinetic constant of the termination step ( $\text{m}^3\cdot\text{mol}^{-1}\cdot\text{s}^{-1}$ )
$k_t^0$	Kinetic constant of the termination step at zero conversion ( $\text{m}^3\cdot\text{mol}^{-1}\cdot\text{s}^{-1}$ )
$k_{ot}$	Kinetic constant of the gel and glass effect on the termination step ( $\text{s}^{-1}$ )
$M$	Monomer
$M_n$	Number-average molecular weight ( $\text{g}\cdot\text{mol}^{-1}$ )
$M_w$	Weight-average molecular weight ( $\text{g}\cdot\text{mol}^{-1}$ )
$M_i^+$	Growing polymer of length $i$
$N_i$	Dead polymer of length $i$
$n_X$	Amount of substance of species $X$ (mol)
$PM_X$	Molecular weight of species $X$ ( $\text{g}\cdot\text{mol}^{-1}$ )
$Q$	Volumetric flow rate ( $\text{m}^3\cdot\text{s}^{-1}$ )
$Q_e$	Monomer input volumetric flow rate ( $\text{m}^3\cdot\text{s}^{-1}$ )
$Q_{er}$	Monomer input volumetric flow rate, excluding the solvent ( $\text{m}^3\cdot\text{s}^{-1}$ )
$R$	Universal gas constant ( $\text{J}\cdot\text{mol}^{-1}\cdot\text{K}^{-1}$ )
$S$	Solvent
$T$	Temperature (K)
$T_{gp}$	Glass temperature (K)
$t$	Time (s)
$U$	Overall heat transfer coefficient ( $\text{J}\cdot\text{s}^{-1}\cdot\text{K}^{-1}\cdot\text{m}^{-2}$ )
$V$	Volume ( $\text{m}^3$ )
$V_{nr}$	Non-reacting volume ( $\text{m}^3$ )
$V_r$	Reacting volume ( $\text{m}^3$ )
$V_{r0}$	Initial reacting volume ( $\text{m}^3$ )
$V_{tot}$	Total volume, including both the reacting and the non-reacting volumes ( $\text{m}^3$ )
$x$	Monomer conversion
$[X]$	Molar concentration of species $X$ ( $\text{mol}\cdot\text{m}^{-3}$ )

(continued on next page)

(continued)

Greek symbols	
$\alpha$	Temperature dependent coefficient of the Fujita-Doolittle equation
$\alpha_{gp}$	Parameter $\alpha$ at glass temperature
$\alpha_T$	Temperature dependency coefficient of parameter $\alpha$ ( $K^{-2}$ )
$\beta$	Constant coefficient of the Fujita-Doolittle equation
$\Delta H_r$	Polymerization reaction enthalpy ( $J\text{-mol}^{-1}$ )
$\epsilon$	Expansion factor
$\Lambda_d$	Pre-exponential factor of the activation step ( $s^{-1}$ )
$\Lambda_i$	Pre-exponential factor of the initiation step ( $m^3\text{-mol}^{-1}\text{-s}^{-1}$ )
$\Lambda_p$	Pre-exponential factor of the propagation step ( $m^3\text{-mol}^{-1}\text{-s}^{-1}$ )
$\Lambda_{op}$	Pre-exponential factor of the gel and glass effect on the propagation step ( $s^{-1}$ )
$\Lambda_{tr}$	Pre-exponential factor of the termination step ( $m^3\text{-mol}^{-1}\text{-s}^{-1}$ )
$\Lambda_{ot}$	Pre-exponential factor of the gel and glass effect on the termination step ( $s^{-1}$ )
$\lambda_k$	$k^{\text{th}}$ statistic moment of the length distribution of the growing polymers
$\mu_k$	$k^{\text{th}}$ statistic moment of the length distribution of the dead polymers
$\rho_X$	Density of species $X$ ( $g\text{-m}^{-3}$ )
$\phi_m$	Monomer fraction in the reacting volume
$\psi$	Generated thermal power ( $J\text{-s}^{-1}$ )
Subscripts	
$e$	Input
$m$	Monomer
$p$	Polymer
$0$	Initial
Superscripts	
*	Activated

### CRedit authorship contribution statement

**Valentín Pérez-Herranz:** Writing – review & editing, Supervision.  
**Montserrat García-Gabaldón:** Writing – review & editing, Supervision.  
**Juan José Giner Sanz:** Writing – original draft, Supervision, Methodology, Data curation, Conceptualization.  
**Fermín Sáez-Pardo:** Writing – original draft, Software, Methodology, Investigation, Data curation, Conceptualization.

### Declaration of Competing Interest

The authors declare that they have no known competing financial interests or personal relationships that could have appeared to influence the work reported in this paper.

### Data availability

Data will be made available on request.

### Acknowledgments

F.S.P. acknowledges the support of Universitat Politècnica de València through a predoctoral fellowship (PAID-01–22). J.J.G.S. is very grateful to the Ministerio de Ciencia e Innovación, to the Next Generation EU, and to the Agencia Estatal de Investigación, for their support by a Juan de la Cierva-Incorporación fellowship IJC2020–044087-I funded by MCIN/AEI/10.13039/501100011033 and by the European Union NextGenerationEU/PRTR. Funding for open access was provided by CRUE-Universitat Politècnica de València.

### References

- Achiliadis, D., Kiparissides, C., 1988. Modeling of diffusion-controlled free-radical polymerization reactions. *J. Appl. Polym. Sci.* 35, 1303–1323. <https://doi.org/10.1002/app.1988.070350516>.
- Achiliadis, D., Kiparissides, C., 1992. Development of a general mathematical framework for modeling diffusion-controlled free-radical polymerization reactions. *Macromolecules* 25, 3739–3750. <https://doi.org/10.1021/ma00040a021>.
- Ahn, S., Chang, S., Rhee, H., 1998. Application of optimal temperature trajectory to batch PMMA. *Polym. React., J. Appl. Polym. Sci.* 69, 59–68. [https://doi.org/10.1002/\(SICI\)1097-4628\(19980705\)69:1<59::AID-APP8>3.0.CO;2-L](https://doi.org/10.1002/(SICI)1097-4628(19980705)69:1<59::AID-APP8>3.0.CO;2-L).
- Ahn, G.N., Taniguchi, S., Aoyama, T., Hasebe, S., Kim, D.P., Tonomura, O., 2020. Formation of gas-liquid slugs in millimeter-scale T-junctions. Slug size estimation framework. *Chem. Eng. J.* 385, 123492. <https://doi.org/10.1016/j.cej.2019.123492>.
- AmPELLI, C., Di Bella, D., Maschio, G., Russo, A., 2006. Calorimetric study of the inhibition of runaway reactions during methylmethacrylate polymerization

- processes. *J. Loss Prev. Proc.* 19, 419–424. <https://doi.org/10.1016/j.jlp.2005.10.003>.
- Arora, S., Gesthuisen, R., Engell, S., 2005. Model based operation of emulsion polymerization reactors with evaporative cooling: application to vinyl acetate homopolymerization. *Comput. -Aided Chem. Eng.* 20, 1255–1260. [https://doi.org/10.1016/S1570-7946\(05\)80051-3](https://doi.org/10.1016/S1570-7946(05)80051-3).
- Arora, P., Jain, R., Mathur, K., Sharma, A., Gupta, A., 2010. Synthesis of polymethyl methacrylate (PMMA) by batch emulsion polymerization. *Afr. J. Pure Appl. Chem.* 4, 152–157.
- Baillagou, P., Soong, D., 1985. Molecular weight distribution of products of free radical nonisothermal polymerization with gel effect. Simulation for polymerization of poly (methyl methacrylate). *Chem. Eng. Sci.* 40, 87–104. [https://doi.org/10.1016/0009-2509\(85\)85049-1](https://doi.org/10.1016/0009-2509(85)85049-1).
- Bao, J., Zou, D., Zhu, S., Ma, Q., Wang, Y., Hu, Y., 2021. A medium-temperature, metal-based, microencapsulated phase change material with a void for thermal expansion. *Chem. Eng. J.* 415, 128965. <https://doi.org/10.1016/j.cej.2021.128965>.
- Baxter, D., Yeh, J., 2012. *The use of polymethyl methacrylate (PMMA) in neurosurgery. Biomaterials for spinal surgery.* Woodhead Publishing, Cambridge, pp. 365–384.
- Bosch, J., Strozzi, F., Lister, D., Maschio, G., Zaldivar, J., 2004. Sensitivity analysis in polymerization reactions using the divergence criterion. *Process Saf. Environ.* 82, 18–25. <https://doi.org/10.1205/09575820432277633>.
- Brydson, J., 1999. *Plastics materials.* Elsevier, Amsterdam.
- Casson, V., Maschio, G., 2011. A calorimetric study of the self-polymerization of a commercial monomer: an incident investigation. *Chem. Eng. Trans.* 24, 1165–1170.
- Casson, V., Snee, T., Maschio, G., 2014. Investigation of an accident in a resins manufacturing site: the role of accelerator on polymerisation of methyl methacrylate. *J. Hazard. Mater.* 270, 45–52. <https://doi.org/10.1016/j.jhazmat.2014.01.038>.
- Cassona, V., Snee, T., Maschio, G., 2014. Effect of amine compounds on the self-polymerisation of methyl methacrylate. *Chem. Eng. Trans.* 36, 109–114. <https://doi.org/10.3303/CET1436019>.
- Chen, T.B., Li, Q.N., Liu, C., Hong, R., Li, Q., Zhu, L., Xu, C., 2021. Hydrophobic fluorinated colloidal photonic crystals for heterogeneous aggregated cluster encoding and energy-saving applications. *Chem. Eng. J.* 411, 128623. <https://doi.org/10.1016/j.cej.2021.128623>.
- Chiu, W., Carratt, G., Soong, D., 1983. A computer model for the gel effect in free-radical polymerization. *Macromolecules* 16, 348–357. <https://doi.org/10.1021/ma00237a002>.
- Copelli, S., Barozzia, M., Petrucci, N., Moreno, V., 2019. Modeling and process optimization of a full-scale emulsion polymerization. *Chem. Eng. J.* 358, 1410–1420. <https://doi.org/10.1016/j.cej.2018.10.055>.
- Copelli, S., Dente, M., Bozzano, G., Barozzi, M., 2018. Simplified modeling and main constitutive parameters estimation for industrial emulsion copolymerization processes. *Chem. Eng. J.* 335, 988–1003. <https://doi.org/10.1016/j.cej.2017.10.181>.
- Copelli, S., Derudi, M., Rota, R., Lunghi, A., Pasturenzi, C., 2011. Experimental design of topological curves to safely optimize highly exothermic complex reacting systems. *Ind. Eng. Chem. Res.* 50, 9910–9917. <https://doi.org/10.1021/ie200017f>.
- Crowley, T., Choi, K., 1996. On-line monitoring and control of a batch polymerization reactor. *J. Process Contr.* 6, 119–127. [https://doi.org/10.1016/0959-1524\(95\)00054-2](https://doi.org/10.1016/0959-1524(95)00054-2).
- Crowley, T., Choi, K., 1997. Calculation of molecular weight distribution from molecular weight moments in free radical polymerization. *Ind. Eng. Chem. Res.* 36, 1419–1423. <https://doi.org/10.1021/ie960623e>.
- Ding, Y., Shi, Y., Nie, J., Ren, Z., Li, S., Wang, F., Tian, J., Chen, X., Wang, Z.L., 2020. Thermochromic triboelectric nanogenerator enabling direct visualization of temperature change during operation. *Chem. Eng. J.* 388, 124369. <https://doi.org/10.1016/j.cej.2020.124369>.
- Duan, C., Liu, Z., Zhu, C., Ma, Y., Fu, T., 2020. Distribution of gas-liquid two-phase flow in parallel microchannels with the splitting of the liquid feed. *Chem. Eng. J.* 398, 125630. <https://doi.org/10.1016/j.cej.2020.125630>.
- Fan, J., Cai, X., Chen, H., Wu, L., Dong, X., Zhang, W., Qiao, Y., Meng, Z., Qiu, L., 2022. A smart large-scale explosive-responsive amorphous photonic crystal sensor based on color analysis method. *Chem. Eng. J.* 446, 136450. <https://doi.org/10.1016/j.cej.2022.136450>.
- Fu, S., Hu, H., Chen, J., Zhu, Y., Zhao, S., 2020. Silicone resin derived larnite/C scaffolds via 3D printing for potential tumor therapy and bone regeneration. *Chem. Eng. J.* 382, 122928. <https://doi.org/10.1016/j.cej.2019.122928>.
- Fujita, H., Kishimoto, A., Matsumoto, K., 1960. Concentration and temperature dependence of diffusion coefficients for systems polymethyl acrylate and n-alkyl acetates. *T. Faraday Soc.* 56, 424–437. <https://doi.org/10.1039/TF9605600424>.
- Gao, J., Penlidis, A., 2002. Mathematical modeling and computer simulator/database for emulsion polymerizations. *Prog. Polym. Sci.* 27, 403–535. [https://doi.org/10.1016/S0079-6700\(01\)00044-2](https://doi.org/10.1016/S0079-6700(01)00044-2).
- Gao, Y., Xiang, H.F., Wang, X.X., Yan, K., Liu, Q., Li, X., Liu, R.Q., Yu, M., Long, Y.Z., 2020. A portable solution blow spinning device for minimally invasive surgery hemostasis. *Chem. Eng. J.* 387, 124052. <https://doi.org/10.1016/j.cej.2020.124052>.
- Ghosh, P., Gupta, S., Saraf, D., 1998. An experimental study on bulk and solution polymerization of methyl methacrylate with responses to step changes in temperature. *Chem. Eng. J.* 70, 25–35. [https://doi.org/10.1016/S1385-8947\(98\)00064-3](https://doi.org/10.1016/S1385-8947(98)00064-3).
- Gil, I., Vargas, J., Corriou, J., 2016. Optimal nonlinear control of an industrial emulsion polymerization reactor. *Chem. Eng. Res. Des.* 111, 63–82. <https://doi.org/10.1016/j.cherd.2016.04.016>.
- Goseki, R., Ishizone, T., 2014. *Poly(methyl methacrylate) (PMMA).* Encyclopedia of Polymeric Nanomaterials. Springer, Berlin.

- Guo, R., Fu, T., Zhu, C., Ma, Y., 2020. Pressure drop model of gas-liquid flow with mass transfer in tree-typed microchannels. *Chem. Eng. J.* 397, 125340 <https://doi.org/10.1016/j.cej.2020.125340>.
- Gygas, R., 1988. Chemical reaction engineering for safety. *Chem. Eng. Sci.* 43, 1759–1771. [https://doi.org/10.1016/0009-2509\(88\)87040-4](https://doi.org/10.1016/0009-2509(88)87040-4).
- Haward, R., 1970. Occupied volume of liquids and polymers. *J. Macromol. Sci. Rev. Macromol. Chem.* 4, 191–242. <https://doi.org/10.1080/15321797008068149>.
- Ibrahim, W.H.B.W., Mujtaba, I.M., Alhamad, B., 2011. Optimization of emulsion copolymerization of styrene and MMA in semi-batch reactor. *Chem. Eng. Trans.* 25, 249–254.
- Kalfas, G., Ray, W., 1993. Modeling and experimental studies of aqueous suspension polymerization processes. 1. Modeling and simulations. *Ind. Eng. Chem. Res.* 32, 1822–1830. <https://doi.org/10.1021/ie00021a005>.
- Kalfas, G., Yuan, H., Ray, W., 1993. Modeling and experimental studies of aqueous suspension polymerization processes. 2. Experiments in batch reactors. *Ind. Eng. Chem. Res.* 32, 1831–1838. <https://doi.org/10.1021/ie00021a006>.
- Kwon, D.K., Myoung, J.M., 2020. Ion gel-based flexible electrochemiluminescence full-color display with improved sky-blue emission using a mixed-metal chelate system. *Chem. Eng. J.* 379, 122347 <https://doi.org/10.1016/j.cej.2019.122347>.
- Law, W., Ibrahim, W., Gimbun, J., 2016. Modeling of methyl methacrylate polymerization using Matlab. *Chem. Prod. Process Mod.* 11, 185–196. <https://doi.org/10.1515/cppm-2015-0070>.
- Li, G., Cheng, R., Cheng, H., Yu, X.Q., Ling, L., Wang, C.F., Chen, S., 2021. Microfluidic synthesis of robust carbon dots-functionalized photonic crystals. *Chem. Eng. J.* 405, 126539 <https://doi.org/10.1016/j.cej.2020.126539>.
- Li, J., Li, H., Liu, Z., Akri, M., Tan, Y., Kang, L., Chi, J., Qiao, B., Ding, Y., 2022a. Synergic effect between gold and vanadate substituted hydroxyapatite support for synthesis of methyl methacrylate by one-step oxidative esterification. *Chem. Eng. J.* 431, 133207 <https://doi.org/10.1016/j.cej.2021.133207>.
- Li, J., Liu, H., Lan, H., Ji, Q., An, X., Liu, R., Qu, J., 2020a. A promising treatment method for Cr (VI) detoxification and recovery by coupling Fe<sup>0</sup>/Fe<sup>3</sup>C/C fine powders and circulating fluidized bed. *Chem. Eng. J.* 398, 125565 <https://doi.org/10.1016/j.cej.2020.125565>.
- Li, Y., Peng, S., Miao, J.T., Zheng, L., Zhong, J., Wu, L., Weng, Z., 2020b. Isotropic stereolithography resin toughened by core-shell particles. *Chem. Eng. J.* 394, 124873 <https://doi.org/10.1016/j.cej.2020.124873>.
- Li, Z., Wang, C., Chen, X., Wang, X., Li, X., Yamauchi, Y., Xu, X., Wang, J., Lin, C., Luo, D., et al., 2020a. MoOx nanoparticles anchored on N-doped porous carbon as Li-ion battery electrode. *Chem. Eng. J.* 381, 122588 <https://doi.org/10.1016/j.cej.2019.122588>.
- Li, J., Yang, L., Zhang, H., Ji, X., 2022b. Self-healing composite solid electrolytes with enhanced Li<sup>+</sup> transport and mechanical properties for safe lithium metal batteries. *Chem. Eng. J.* 438, 135418 <https://doi.org/10.1016/j.cej.2022.135418>.
- Liu, M., Guan, X., Liu, H., Ma, X., Wu, Q., Ge, S., Zhang, H., Xu, J., 2022. Composite solid electrolytes containing single-ion lithium polymer grafted garnet for dendrite-free, long-life all-solid-state lithium metal batteries. *Chem. Eng. J.* 445, 136436 <https://doi.org/10.1016/j.cej.2022.136436>.
- Louie, B., Carratt, G., Soong, D., 1985. Modeling the free radical solution and bulk polymerization of methyl methacrylate. *J. Appl. Polym. Sci.* 30, 3985–4012. <https://doi.org/10.1002/app.1985.070301004>.
- Ma, Y., Gou, T., Feng, C., Li, J., Li, Y., Huang, J., Li, R., Zhang, Z., Gao, X., 2021. Facile fabrication of biomimetic films with the microdome and tapered nanonipple hierarchical structure possessing high haze, high transmittance, anti-fouling and moisture self-cleaning functions. *Chem. Eng. J.* 404, 127101 <https://doi.org/10.1016/j.cej.2020.127101>.
- Mao, P., Sun, Q., Zhang, L., Wang, Z., He, L., Kang, R., Lu, G., Xie, B., Liu, Z., Wang, J., 2022. Multilayer-structured nanocomposite films with enhanced energy storage performance under intermediate electric fields via incorporation of BaTiO<sub>3</sub>/CaCu<sub>3</sub>Ti<sub>4</sub>O<sub>12</sub>@ SiO<sub>2</sub> nanofillers. *Chem. Eng. J.* 431, 134320 <https://doi.org/10.1016/j.cej.2021.134320>.
- Marien, Y., Edeleva, M., Figueira, F., Arraez, F., Van Steenberge, P., D'hooge, D., 2021. Translating simulated chain length and molar mass distributions in chain-growth polymerization for experimental comparison and mechanistic insight. *Macromol. Theor. Simul.* 30, 2100008. <https://doi.org/10.1002/mats.202100008>.
- Marten, F., Hamielec, A., 1979. High conversion diffusion-controlled polymerization, *Polymerization Reactors and Processes 104*. ACS Symposium Series. A.C. Society, Washington DC, pp. 43–70.
- Moreno, V., Tugnoli, A., Salzano, E., Cozzani, V., 2016. Escalation scenarios triggered by thermal explosions in batch and semi-batch reactors. *Chem. Eng. Trans.* 48, 463–468. <https://doi.org/10.3303/CET1648078>.
- P. Nising, High-temperature radical polymerization of methyl methacrylate in a continuous pilot scale process, Lausanne (Switzerland), 2006.
- Nolan, P., Barton, J., 1987. Some lessons from thermal-runaway incidents. *J. Hazard. Mater.* 14, 233–239. [https://doi.org/10.1016/0304-3894\(87\)87015-2](https://doi.org/10.1016/0304-3894(87)87015-2).
- Pokorný, R., Zubov, A., Matuška, P., Lueth, F., Pauer, W., Moritz, H., Kosek, J., 2016. Process model for styrene and n-butyl acrylate emulsion copolymerization in smart-scale tubular reactor. *Ind. Eng. Chem. Res.* 55, 472–484. <https://doi.org/10.1021/acs.iecr.5b02909>.
- Poling, B., Prausnitz, J., O'Connell, J., 2001. *The properties of gases and liquids*, 5th edition ed. McGraw-Hill, New York.
- Prentice, P., 1983. Influence of molecular weight on the fracture of poly(methyl methacrylate) (PMMA). *Polymer* 24, 344–350. [https://doi.org/10.1016/0032-3861\(83\)90275-6](https://doi.org/10.1016/0032-3861(83)90275-6).
- Rawlings, J., Ray, W., 1988. The modeling of batch and continuous emulsion polymerization reactors. Part II: comparison with experimental data from continuous stirred tank reactors. *Polym. Eng. Sci.* 28, 257–274. <https://doi.org/10.1002/pen.760280503>.
- Ren, L.F., Ngo, H.H., Bu, C., Ge, C., Ni, S.Q., Shao, J., He, Y., 2020. Novel external extractive membrane bioreactor (EMBR) using electrospon polydimethylsiloxane/polymethyl methacrylate membrane for phenol-laden saline wastewater. *Chem. Eng. J.* 383, 123179 <https://doi.org/10.1016/j.cej.2019.123179>.
- Serrano-Aroca, A., Deb, S., 2020. Acrylate polymers for advanced applications. *IntechOpen, London*.
- Shahrokhi, M., Fanaei, M., 2002. Nonlinear temperature control of a batch suspension polymerization reactor. *Polym. Eng. Sci.* 42, 1296–1308. <https://doi.org/10.1002/pen.11032>.
- Sheu, W., 2001. Molecular weight averages and polydispersity of polymers. *J. Chem. Educ.* 78, 554–555. <https://doi.org/10.1021/ed078p554>.
- Stepito, R., 2009. Dispersity in polymer science. *Pure Appl. Chem.* 81, 351–353. <https://doi.org/10.1351/PAC-REC-08-05-02>.
- M. Stickler, R. Rhein, *Polymethacrylates*, Ullmann's Encyclopedia of Industrial Chemistry, New York, 1992.
- Sun, H., Liu, Y., Guo, X., Zeng, K., Mondal, A.K., Li, J., Yao, Y., Chen, L., 2021. Strong, robust cellulose composite film for efficient light management in energy efficient building. *Chem. Eng. J.* 425, 131469 <https://doi.org/10.1016/j.cej.2021.131469>.
- Suzuki, Y., Cousins, D., Wassgren, J., Kappes, B., Dorgan, J., Stebner, A., 2018. Kinetics and temperature evolution during the bulk polymerization of methyl methacrylate for vacuum-assisted resin transfer molding. *Compos. Part A - Appl. S.* 104, 60–67. <https://doi.org/10.1016/j.compositesa.2017.10.022>.
- Tefera, N., Weickert, G., Westertep, K., 1997. Modeling of Free radical polymerization up to high conversion. II. Dev. a Math. Model J. Appl. Polym. Sci. 63, 1663–1680. [https://doi.org/10.1002/\(SICI\)1097-4628\(19970321\)63:12<1663::AID-APP17>3.0.CO;2-0](https://doi.org/10.1002/(SICI)1097-4628(19970321)63:12<1663::AID-APP17>3.0.CO;2-0).
- Teja, A., 1983. Simple method for the calculation of heat capacities of liquid mixtures. *J. Chem. Eng. Data* 28, 83–85. <https://doi.org/10.1021/je00031a025>.
- Tobolsky, A., Baysal, B., 1953. A review of rates of initiation in vinyl polymerization: styrene and methyl methacrylate. *J. Polym. Sci.* 11, 471–486. <https://doi.org/10.1002/pol.1953.120110509>.
- Wang, H., Wu, J., Song, J., Qu, J., Lian, J., Qian, P.C., Wong, W.Y., 2021. Conjugated polyelectrolyte doped perovskite films with enhanced photovoltaic performance and stability. *Chem. Eng. J.* 417, 128068 <https://doi.org/10.1016/j.cej.2020.128068>.
- Wu, J., Shan, G., 2006. Kinetic and molecular weight control for methyl methacrylate semi-batch polymerization. I. Modelling. *J. Appl. Polym. Sci.* 100, 2838–2846. <https://doi.org/10.1002/app.23792>.
- Xie, A.Q., Guo, J., Zhu, L., Chen, S., 2021. Carbon dots promoted photonic crystal for optical information storage and sensing. *Chem. Eng. J.* 415, 128950 <https://doi.org/10.1016/j.cej.2021.128950>.
- Xu, G., Wang, B., Song, S., Ren, Z., Li, J., Xu, X., Zhou, W., Li, H., Yang, H., Zhang, L., 2021. et al., High-performance and robust dual-function electrochromic device for dynamic thermal regulation and electromagnetic interference shielding. *Chem. Eng. J.* 422, 130064 <https://doi.org/10.1016/j.cej.2021.130064>.
- Zhan, Z., Wang, L., Duan, R., Shi, Q., Shen, J., Weng, S., Wang, X., Yan, L., Zhang, B., Li, L., 2022. A novel strategy to improve the flame retardancy and electrical conductivity of polymethyl methacrylate by controlling the configuration of phosphorus-containing polyaniline@ needle coke with magnetic field, 2022 *Chem. Eng. J.* 448, 137642. <https://doi.org/10.1016/j.cej.2022.137642>.
- Zhang, S., Cagney, N., Lacassagne, T., Balabani, S., Naveira-Cotta, C., Tiwari, M., 2020. Mixing in flows past confined microfluidic cylinders: effects of pin and fluid interface offsetting. *Chem. Eng. J.* 397, 125358 <https://doi.org/10.1016/j.cej.2020.125358>.
- Zhao, F., Chen, Z., Fan, W., Dou, J., Li, L., Guo, X., 2020. Reactor optimization and process intensification of photocatalysis for capillary-based PMMA LSC-photomicroreactors. *Chem. Eng. J.* 389, 124409 <https://doi.org/10.1016/j.cej.2020.124409>.
- Zhao, H., Deng, N., Wang, G., Ren, H., Kang, W., Cheng, B., 2021. A core sheath nanofiber separator with combined hardness and softness for lithium-metal batteries. *Chem. Eng. J.* 404, 126542 <https://doi.org/10.1016/j.cej.2020.126542>.
- Zhou, Z., Feng, Y., Wang, J., Liang, B., Li, Y., Song, Z., Itkis, D., Song, J., 2020. A robust, highly stretchable ion-conductive skin for stable lithium metal batteries. *Chem. Eng. J.* vol. 396, 125254 <https://doi.org/10.1016/j.cej.2020.125254>.
- Zubov, A., Pokorný, J., Kosek, J., 2012. Styrene-butadiene rubber (SBR) production by emulsion polymerization: dynamic modeling and intensification of the process. *Chem. Eng. J.* 207, 414–420. <https://doi.org/10.1016/j.cej.2012.06.144>.